OXFORD

Journal of Petrology, 2023, **64**, 1–23
https://doi.org/10.1093/petrology/egac128
Advance access publication date 23 December 2022
Original Manuscript

Reaction-Induced Porosity in an Eclogite-Facies Vein Selvage (Monviso Ophiolite, W. Alps): Textural Evidence and *In Situ* Trace Elements and Sr Isotopes in Apatite.

William F Hoover [1,*], Sarah Penniston-Dorland [1], Philip Piccoli[1] and Andrew Kylander-Clark [2]

[1]Department of Geology, University of Maryland, College Park, MD, 20742, USA
[2]Department of Earth Science, University of California, Santa Barbara, CA, 93106, USA
*Corresponding author. Present Address: Department of Earth and Space Science, University of Washington, Seattle, WA, 98195, USA. Telephone: +1 717 462 0055. E-mail: wfhoover@uw.edu

Abstract

Porosity generated during fluid–rock reaction can facilitate fluid transport and metasomatism in low permeability high-pressure metamorphic rocks. Evidence for reaction-induced porosity is found in an eclogite-facies clinopyroxene + apatite vein in an undeformed eclogitized Fe–Ti metagabbro from the Monviso Ophiolite (W. Alps) with a distinct garnet-rich selvage. Vein-forming fluids were sourced from adjacent metagabbros and reaction with the host rock removed Ca and P from the selvage and added Fe, REE, Pb and Cr. Textures at the selvage–host rock interface and in the host rock record local heterogeneity in reactivity and porosity during metasomatism linked to variable initial lawsonite abundance. These features reflect a hierarchy of pervasive-to-channelized porosity structures that facilitated widespread metasomatism of the host rock. Development of this metasomatic system in response to locally derived fluids suggests large-scale externally derived fluid transport is not required to drive extensive fluid–rock exchange. The production of porosity during metasomatic reactions could be important in facilitating further fluid–rock reaction and fluid transport in subducting slabs where permeability is low.

Keywords: Sr isotopes, porosity, Alps, apatite, eclogite

INTRODUCTION

Subduction zones are fluid-rich environments that witness extensive metasomatism between juxtaposed lithologies (e.g. ultramafic rocks and oceanic sediments) and during fluid transport (e.g. Sorensen & Barton, 1987; Bebout & Barton, 2002; Breeding *et al.*, 2004; Spandler *et al.*, 2008; Miller *et al.*, 2009; Beinlich *et al.*, 2010; Spandler *et al.*, 2011; Bebout & Penniston-Dorland, 2016; Piccoli *et al.*, 2016; Taetz *et al.*, 2016; Gyomlai *et al.*, 2021; van Schrojenstein Lantman *et al.*, 2021). The application of new isotope systems (Li, K, Mg, Fe, Zn, Cl; e.g. Penniston-Dorland *et al.*, 2010; Inglis *et al.*, 2017; Li *et al.*, 2018; Barnes *et al.*, 2019; Wang *et al.*, 2022) and high-spatial resolution geochemical analysis (e.g. secondary ion mass spectrometry; Errico *et al.*, 2013; Rubatto & Angiboust, 2015; Bovay *et al.*, 2021; Cruz-Uribe *et al.*, 2021; Hoover *et al.*, 2022) provides a more nuanced understanding of fluid–rock reaction and fluid transport in subduction zones. These methods have highlighted the prevalence of cryptic metasomatism, in which rocks that otherwise show little macroscopic or petrographic evidence of metasomatism or fluid infiltration have been geochemically modified. For example, in subduction zone mélanges, oxygen isotope zoning in garnet from 'unaltered' blocks, well beyond the extent of reaction rind formation, is consistent with infiltration of externally derived fluids into the cores of these blocks (e.g. Errico *et al.*, 2013; Page *et al.*, 2014; Hoover *et al.*, 2020). Similarly, large ion lithophile element enrichment and kinetically fractionated Li isotope ratios in mélange block cores suggest prior diffusive metasomatism although mineralogically, the blocks appear to be 'pristine' metamafic rocks (e.g. Sorensen *et al.*, 1997; Penniston-Dorland *et al.*, 2012). This evidence of cryptic metasomatism suggests that fluid infiltration can be extensive at the m-scale in subducted metamafic rocks despite their nominally low porosity (e.g. Angiboust & Raimondo, 2022) and lack of major element metasomatism or mineralogical change.

Field, geochemical, experimental and modeling studies of mineral replacement and dehydration, on the other hand, have highlighted the potential importance of micro- and nano-scale porosity, particularly developed during mineral reactions, in controlling fluid in- and ex-filtration (e.g. van der Straaten *et al.*, 2008; Putnis & Austrheim, 2011; John *et al.*, 2012; Jonas *et al.*, 2014; Plümper *et al.*, 2017; Konrad-Schmolke *et al.*, 2018). These new grain-boundary-scale fluid transport pathways could facilitate cryptic metasomatism. However, identification of widespread nano- and micro-scale fluid transport networks in the rock record remain rare (e.g. channel-forming porosity draining dehydrating antigorite; Plümper *et al.*, 2017), as do characterizations of the conditions under which they can form. Here we present results from a textural and geochemical study of an eclogite-facies vein, reaction selvage and host rock from the Monviso Ophiolite (W. Alps) to investigate the extent of reaction-induced porosity development and its metasomatic impact.

Received: April 28, 2022. **Revised:** December 13, 2022

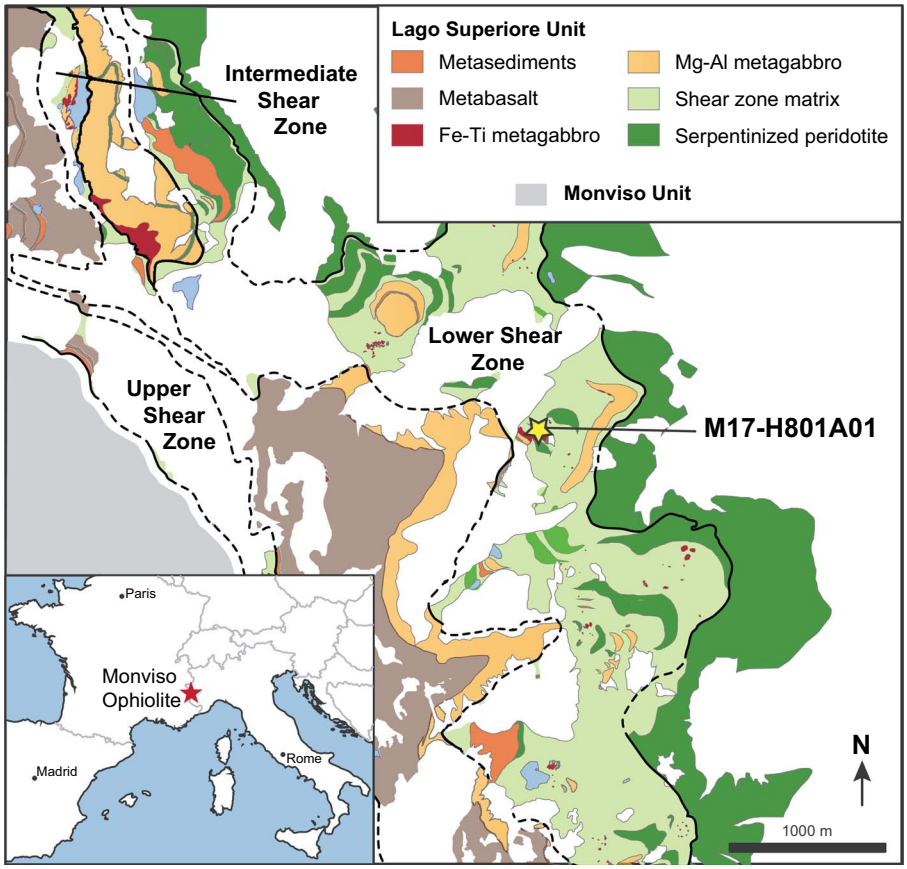

Fig. 1. Lithologic map of the Monviso Ophiolite modified from Locatelli *et al.* (2019a) showing the intact oceanic crustal structure of the Lago Superiore Unit. Dashed lines mark the extent of ultramafic-dominated shear zones separating lithologic layers. The studied sample (M17-H801A01) is marked by the star and was taken from an outcrop of unbrecciated Fe–Ti metagabbro with the LSZ.

GEOLOGIC BACKGROUND

The Lago Superiore Unit of the Monviso Ophiolite is a mafic-rich slice of hyper-extended oceanic lithosphere in the Western Alps metamorphosed at eclogite-facies during subduction beneath Apulia (modern-day Italy; e.g. Lombardo *et al.*, 1978; Beltrando *et al.*, 2010; Locatelli *et al.*, 2019a; Agard, 2021). The Lago Superiore Unit is made up of a preserved oceanic lithosphere section with serpentinized lherzolitic mantle overlain by metagabbro, metabasalt and a thin veneer of metamorphosed pelitic sediments (Fig. 1; e.g. Lombardo *et al.*, 1978; Angiboust *et al.*, 2012b; Locatelli *et al.*, 2019a). Geochronology (U–Pb zircon, Lu-Hf and Sm-Nd garnet) is consistent with an oceanic crust protolith that formed in a hyperextended ocean basin in the Jurassic and underwent eclogite-facies metamorphism around 45 Ma (e.g. Lombardo *et al.*, 1978; Duchêne *et al.*, 1997; Cliff *et al.*, 1998; Rubatto & Hermann, 2003; Festa *et al.*, 2015; Rubatto & Angiboust, 2015). Reported peak metamorphic pressure–temperature conditions for the Lago Superiore Unit range from 1.9 to 2.8 GPa and 545 to 650 °C (Messiga *et al.*, 1999; Schwartz *et al.*, 2000; Castelli *et al.*, 2002; Groppo & Castelli, 2010; Angiboust *et al.*, 2012b; Locatelli *et al.*, 2018), but were shown to be internally consistent by Angiboust *et al.* (2012b). Peak metamorphic mineral assemblages are best preserved in the metagabbroic layer of the ophiolite, which is composed of volumetrically dominant Mg–Al gabbro and lenses and dikes of Fe–Ti gabbro. Both types of metagabbro are also found as blocks within ultramafic shear zones (Fig. 1; e.g. Angiboust *et al.*, 2011; Angiboust *et al.*, 2014; Locatelli *et al.*, 2019a).

Eclogite-facies omphacite veins are commonly observed cutting mylonitized Fe–Ti metagabbro blocks and layers (Philippot, 1987). These veins formed concurrent with ductile deformation immediately prior to peak metamorphism (~2.6 GPa, 550 °C; Locatelli *et al.*, 2018). Where deformation was minimal, prograde fluid release resulted in the formation of fluid-filled vugs (~4% porosity) that retained fluid over million-year timescales due to extremely low permeability (Angiboust & Raimondo, 2022). Bulk oxygen isotope ratios measured in host rocks and veins were consistent with fluids sourced within centimeters of veins (Nadeau *et al.*, 1993). More recent geochemical studies identified two generations of vein material based on bulk and omphacite Cr concentration (Spandler *et al.*, 2011). In many vein minerals, trace element concentrations and Hf isotopes are comparable to those in the host rock, consistent with the interpreted local fluid source (Spandler *et al.*, 2011). However, a subpopulation of vein minerals (omphacite, rutile and garnet) is enriched in Cr, as well as Ni, B, As, Sb, Nb, Zr and LREE/MREE (Spandler *et al.*, 2011). This subpopulation was interpreted as evidence of periodic large-scale serpentinite-derived fluid transport through a network of veins originally developed to transport locally derived fluids.

Many Fe–Ti eclogite mylonite blocks within the upper portion of the Lower Shear Zone (LSZ), and less commonly within the Intermediate Shear Zone, contain three generations of eclogite breccias cross-cutting omphacite veins (Angiboust *et al.*, 2012a; Locatelli *et al.*, 2018; Locatelli *et al.*, 2019b). Brecciation began at peak metamorphism (~2.7 GPa, 580 °C) and continued through initial of exhumation (<2.4 GPa, <560 °C; Locatelli *et al.*, 2018). Brecciation under eclogite-facies conditions is confirmed by the

Table 1: Summary of results from Locatelli *et al.* (2019b) outlining chemical changes and inferred fluid sources for veins and eclogite breccia matrices in the Monviso Ophiolite

Chronology	Feature	Location	Fluid source	Mineralogy	Trace element signature
earliest	V0	LSZ + ISZ	Fe–Ti	Omp ± Ap	+Y,HREE
	V1	LSZ + ISZ	Fe–Ti + Int	Omp + Ap	+Cr,Ni,Co,Pb,Sr
	M1	LSZ	Mg–Al + Int	Omp + Ap	+Cr,Ni,Co,Pb,Sr
	V2	ISZ	Mg–Al + Serp	Omp + Grt ± Ap	++Cr,Ni,Co,Pb,Sr
	M2	LSZ + ISZ	Mg–Al + Serp	Omp + Grt + Ap	++Cr,Ni,Co,Pb,Sr
latest	M3	LSZ	Serp	Lws + Omp + Tlc + Chl ± Rt	+++Cr,Ni,Co -HFSE,LILE

V = vein; M = matrix; LSZ = Lower Shear Zone; ISZ = Intermediate Shear Zone; Int = Intermediate metagabbro (garnet-bearing Mg–Al metagabbro)

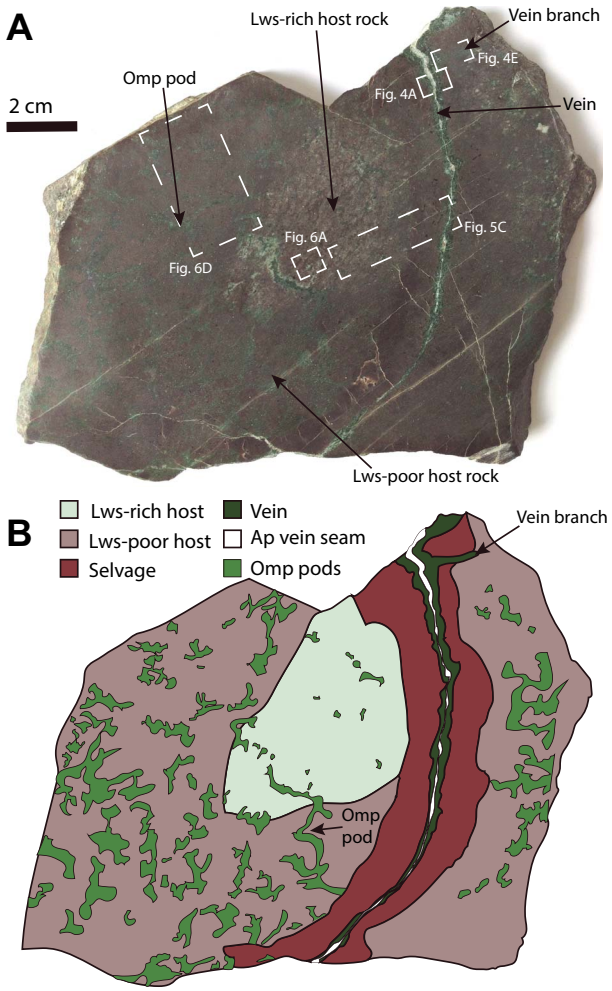

Fig. 2. (A) Hand sample photo of M17-H801A01. (B) Interpretive overlay on (A) showing the vein, selvage, bimodal host rock mineralogy and the distribution of omphacite pods visible in hand sample. White dashed boxes show the approximate location of large-scale photomicrographs in following figures. Abbreviations are Omp, omphacite; Ap, apatite; Lws, lawsonite, from Whitney & Evans (2010).

rotation of mylonitic foliation and the truncation and offset of garnet porphyroblasts across clast boundaries (Locatelli *et al.*, 2018). Brecciation is interpreted to have involved fluid transport and transient high pore-fluid pressures and successive breccia matrix generations progress from geochemical signatures of local, gabbro-derived to external, serpentinite-derived fluid (Locatelli *et al.*, 2019b). Vein generations associated with this brecciation record a similar evolution of inferred fluid source and have been proposed as nucleation sites for brecciation (Locatelli *et al.*, 2019b). Initial influx of locally derived fluids involved modest additions of Y + HREE (Fe–Ti metagabbro source) and Cr, Ni, Co, Pb and Sr (~2× increase; intermediate metagabbro source), limited change in omphacite major element compositions, and veins and breccia matrix mineralogy of omphacite + apatite. Increased contributions from Mg–Al and serpentinite derived fluids drove significant enrichments (10–20×) in Cr, Ni and Co and changes in omphacite composition, and yielded omphacite + garnet + apatite and lawsonite-dominated veins and breccia matrices (Table 1; Locatelli *et al.*, 2019b). The more discrete Cr-rich and Cr-poor vein compositions measured in omphacite veins unassociated with breccia may record a related fluid history (Spandler *et al.*, 2011; Locatelli *et al.*, 2019b).

SAMPLE DESCRIPTION

The sample presented here is an Fe–Ti metagabbro collected within the LSZ near Punta Forcion (Fig. 1; sample ID: M17-H801A01, IGSN: EXT000023, 44°40.620′ N, 007°07.551′ E). The ultramafic matrix of the LSZ is rarely preserved in contact with resistant metagabbro blocks complicating identification of in-place blocks versus float. The sampled outcrop contained no bounding contacts and cannot be definitively identified as in-place. However, adjacent outcrops on the multi-meter scale contain similar fine-grained, unbrecciated Fe–Ti metagabbro with large apatite and rutile crystals suggesting some local coherence.

The sample itself is a fine-grained (dominantly <500 μm) eclogite-facies Fe–Ti metagabbro cut by a clinopyroxene and apatite vein (Fig. 2). The vein is separated from the host rock by an alteration selvage ~1.5 cm thick. The peak mineral assemblage of the host rock is garnet + omphacite + lawsonite + rutile + apatite (Table 2 and Fig. 3). Clinozoisite, phengite and quartz are found together, often in tabular shaped aggregates, and have previously been interpreted as pseudomorphs after lawsonite (Fig. 4A and B; Angiboust *et al.*, 2011). In this sample, albite and titanite are often associated with these pseudomorphs and are interpreted as retrograde alteration (Figs. 3B and 4B). The host rock exposed within the sample can be divided into lawsonite-rich and lawsonite-poor domains based on the abundance of pseudomorphs after lawsonite (Table 2, Figs. 2 and 3). Throughout the manuscript we use 'omphacite' and 'magnesian augite' specifically when referring to portions of the sample where clinopyroxene is exclusively of that composition, while clinopyroxene is used inclusively when referred to portions of the sample with multiple clinopyroxene compositions.

LAWSONITE-RICH HOST ROCK

The lawsonite-rich domain of the host rock (Lws-rich) is dominated by <100 μm intergrowths of omphacite, lawsonite (now

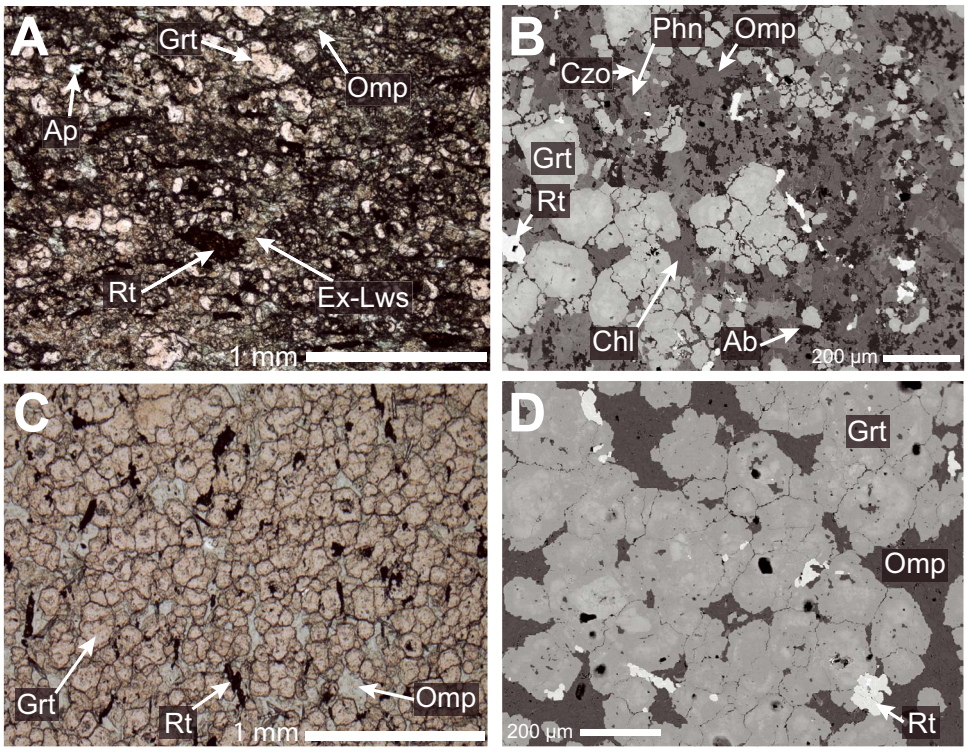

Fig. 3. Images of the two host rock domains. (A) Plane-polarized light photomicrograph showing the typical mineral assemblage of the lawsonite-rich host rock domain. (B) Back-scattered electron image of the lawsonite-rich host rock domain showing the intergrowth of omphacite and former lawsonite. (C) Plane-polarized light photomicrograph showing the typical mineral assemblage of the lawsonite-poor host rock domain. (B) Back-scattered electron image of the lawsonite-poor host rock showing the absence of pseudomorphs after lawsonite or apatite in the matrix.

Table 2: Mineralogical and textural summary of the studied sample

Domain	Cpx	Grt	Czo*	Ap	Rt	Chl	Ab**	Phn**	Zrn	Aln	Omphacite pods
Vein	+++	tr		+	tr						
Vein seam	+			+++	tr		tr	tr			
Selvage	++	++(+)	++		+	tr	psd	psd			rare
Lws-poor host rock	++	+++	tr	incl	+	tr	psd	psd	tr	tr	abundant
Lws-rich host rock	++	++	+++	+	+	tr	psd	psd	tr	tr	common
Omphacite pods	+++		+	+			psd	psd	tr		

Visually estimated relative mineral modes: +++ >50%, ++ > 15%, + >5%, tr, trace; psd, present in lawsonite pseudomorphs; incl, garnet inclusion. Abbreviations from Whitney & Evans (2010).
*dominant mineral in pseudomorphs after lawsonite and used to infer lawsonite abundance.
**subordinate mineral in lawsonite pseudomorphs outside the vein.

pseudomorphed by clinozoisite and phengite) and chlorite, with subordinate garnet, accessory rutile and apatite, and trace allanite and zircon (Table 2 and 3, Fig. 3A and B). Clinozoisite and phengite are found together with rare paragonite and quartz and interpreted to be former lawsonite (Ex-Lws; Angiboust *et al.*, 2011), although the abundance of these phases obscures clear tabular shapes (Fig. 3A and B). Garnet inclusions are uncommon and typically rutile, apatite, omphacite, chlorite and quartz. Retrograde albite and possibly chlorite are found in the matrix intergrown with omphacite and former lawsonite. However, inclusions of chlorite in garnet suggest that some chlorite may be a peak phase consistent with previous work (Angiboust *et al.*, 2014; Hoover *et al.*, 2022).

LAWSONITE-POOR HOST ROCK

The lawsonite-poor domain of the host rock is dominated by garnet with subordinate omphacite and rutile and trace chlorite, zircon, allanite and pseudomorphs after lawsonite (Table 2, Fig. 3C and D). Former lawsonite in the Lws-poor host rock occurs as distinct tabular shapes containing poikiloblastic clinozoisite, phengite, quartz and titanite, possible former inclusions of omphacite, garnet, rutile, apatite and zircon inherited from lawsonite and retrograde albite (Fig. 4A and B). Inclusions within garnet are found in distinct concentric bands that contain omphacite, rutile, sulfide, apatite, phengite and quartz. While common as inclusions in garnet, apatite is not found in the matrix of the Lws-poor host.

VEIN

Both the Lws-rich and -poor domains are crosscut by the single clinopyroxene + apatite vein that traverses the entire sample (Table 2, Figs. 2 and 5). The vein is tabular and gently curved and tapers from ~10 mm thickness at one side of the sample to ~3 mm at the other (Fig. 2). While the vein is dominated by clinopyroxene (Fig. 5D), a discontinuous seam of apatite is found in the center of the vein (Fig. 5A, B and C). Omphacite in the main body of the vein is 200 to 500 μm in length with distinct length-parallel linear

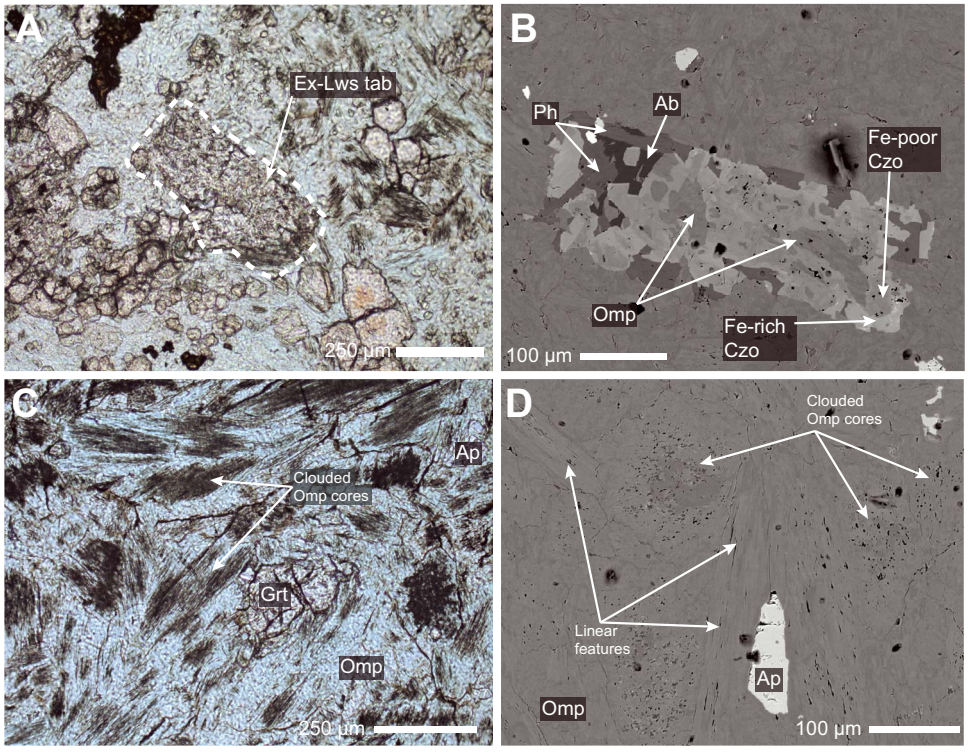

Fig. 4. Detailed images of lawsonite pseudomorph and omphacite textures. (A) Plane-polarized light photomicrograph of a tabular lawsonite pseudomorph (Ex-Lws) in the lawsonite-poor host rock. (B) Back-scattered electron image of a lawsonite pseudomorph showing the complex mineralogy and poikiloblastic texture of these breakdown products. (C) Plane-polarized light photomicrograph of the coarse omphacite texture characteristic of the vein and omphacite pods (omphacite in the vein). Garnet in the image is the only garnet crystal identified in the vein and shown in Fig. 8C. (D) Back-scattered electron image of coarse omphacite in an omphacite pod showing the characteristic core clouded by linear features.

features clouding crystal cores (termed coarse omphacite; Figs. 4C and D, 5D). Clinopyroxene crystals have no preferred orientation to the vein wall (Fig. 5D). Large apatite crystals and rare garnet and rutile are found within the omphacite-dominated portion of the vein (Table 2, Figs. 4C and 5D). The boundary between the vein and associated selvage is marked by a textural change from coarse omphacite (>200 μm in length) to fine-grained equant omphacite <100 μm in size (Figs. 5E and 6A). Rare branches of coarse omphacite extend from the main vein and traverse across the alteration selvage (Figs. 2 and 5E).

Apatite seam

The apatite seam in the main vein is discontinuous and pinches and swells along its length (Figs. 2 and 5A, B and C). Apatite in the seam is blocky and massive, with individual crystals 200 μm to several millimeters in dimension (Fig. 5C). Rutile needles up to 3 cm in length are observed within the seam in hand sample, and large inclusions of rutile are observed in thin section (Table 2, Fig. 5B). Small acicular inclusions of clinopyroxene 5 to 50 μm in length are distributed throughout the apatite seam, and larger needles up to hundreds of microns in length are found radiating from a band of inclusions that runs the length of the seam in thin section (Fig. 5B and C).

VEIN SELVAGE

The main clinopyroxene + apatite vein crosscutting the studied sample is separated from the host rock by an alteration selvage ~1.5 cm thick (Figs. 2 and 6A, B, C and D). This selvage separates the clinopyroxene + apatite vein from both the Lws-rich and Lws-poor host rock domains and is distinguished from both by mineral abundance. The selvage mineral assemblage developed between the Lws-rich host rock and the vein is omphacite, garnet, rutile, pseudomorphs after lawsonite and chlorite with significant internal modal variability (Table 2 and 3, Fig. 6C, D and E). The selvage is best distinguished from both host rock regions by clinopyroxene abundance, higher than the Lws-rich host rock and lower than the Lws-poor host rock, and distinct textures that bound the selvage. On the vein-side, the selvage is bounded by a region of fine-grained omphacite (<100 μm) and a sharp transition to the coarse omphacite of the vein (Fig. 6A). On the opposite side of the selvage, at the boundary with the host rock, the selvage is characterized by a near-monomineralic zone of garnet of varying thickness composed of intergrown multi-crystal aggregates (garnetite; Fig. 6B, C, D and E). The selvage–host rock boundary is undulose with peninsulas of garnetite that penetrate the host rock up to 1.5 mm beyond the main boundary (Fig. 6B). Former lawsonite (dominantly clinozoisite) is rare in the selvage and is concentrated in irregular regions that never approach the abundance in the Lws-rich host rock (Fig. 6E). Apatite is a trace phase within the selvage (Table 3 and Fig. 6D).

OMPHACITE PODS

Omphacite-rich pods are distributed throughout the Lws-rich and Lws-poor host rock domains as well as the selvage forming a discontinuous network (Fig. 7). These pods are distinguished from the surrounding host rock by the presence of coarse omphacite with cores clouded by aligned linear features (Figs. 4C and D, and 7). In hand sample, laterally extensive pods in the Lws-poor host rock can be traced as continuous with those in the Lws-rich portion of the host rock suggesting a shared origin (Fig. 2).

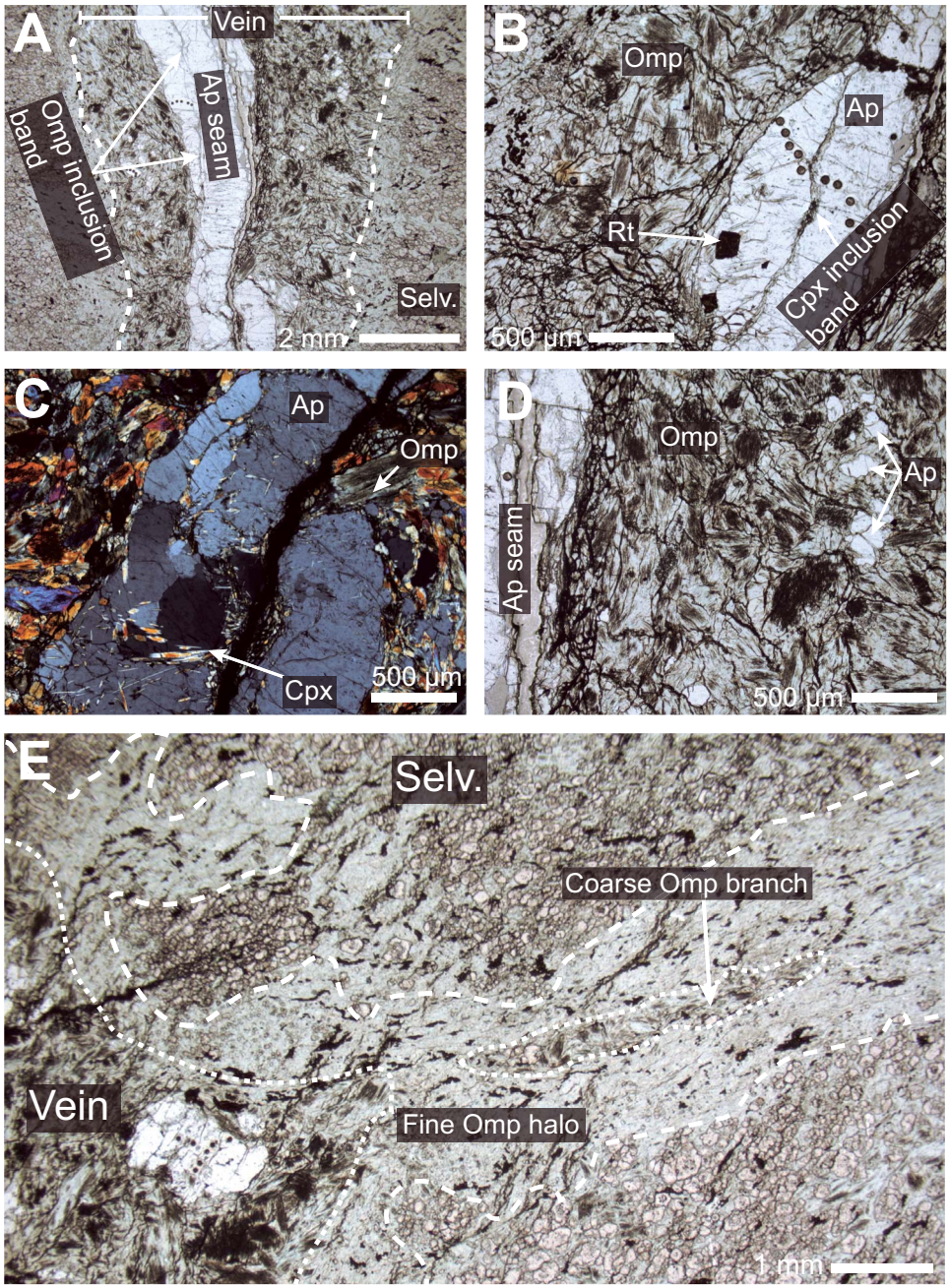

Fig. 5. Photomicrographs of the clinopyroxene + apatite vein. (A) Plane-polarized light photomicrograph of the apatite vein showing the clinopyroxene vein and apatite seam. The edge of the vein is defined by the transition from coarse omphacite to fine-grained omphacite. (B) Plane-polarized light photomicrograph of the apatite seam showing inclusions of clinopyroxene and rutile. (C) Cross-polarized light photomicrograph of the apatite seam showing the numerous acicular clinopyroxene inclusions. (D) Plane-polarized light photomicrograph of the main body of the vein showing the coarse omphacite texture and non-seam apatite. (E) Plane-polarized light photomicrograph of a vein branch spanning the selvage and bounded by fine-grained omphacite similar to the main vein. Coarse omphacite is discontinuous but found along the center of much of this branch. This vein branch traverses the entire selvage. Abbreviation: Cpx, clinopyroxene, from Whitney & Evans (2010).

In all host rock domains, omphacite pods are elongate but rarely linear, characterized by curved, branching or sinuous topology (Fig. 7). Pods are typically 0.25 to 10 mm in length and have aspect ratios ranging from 2:1 to 20:1 (Fig. 7). In the Lws-poor host rock, omphacite pods are larger, more abundant, and more laterally continuous and interconnected (sometimes for >1 cm) than in the Lws-rich host rock (Fig. 7D, E and F). In the Lws-poor host rock, pods sometimes contain large apatite crystals and rare garnet, chlorite and pseudomorphs after lawsonite in addition to coarse omphacite (Figs. 4A, 7D, E and F). In the host rock matrix around pods, large apatite and lawsonite pseudomorphs are nearly absent. The largest pods in the Lws-poor host rock are surrounded by halos of fine-grained omphacite similar to that at the vein–selvage contact (Fig. 7E). Pods in the Lws-rich host rock commonly contain garnet, and apatite, but never contain pseudomorphs after lawsonite (Fig. 7A, B and C). Both garnet and apatite in omphacite pods of the Lws-rich host rock are significantly larger than that found in the surrounding matrix (Fig. 7B and C). Omphacite pods in the selvage are similar to those in the Lws-poor host rock and occur at a range of orientations

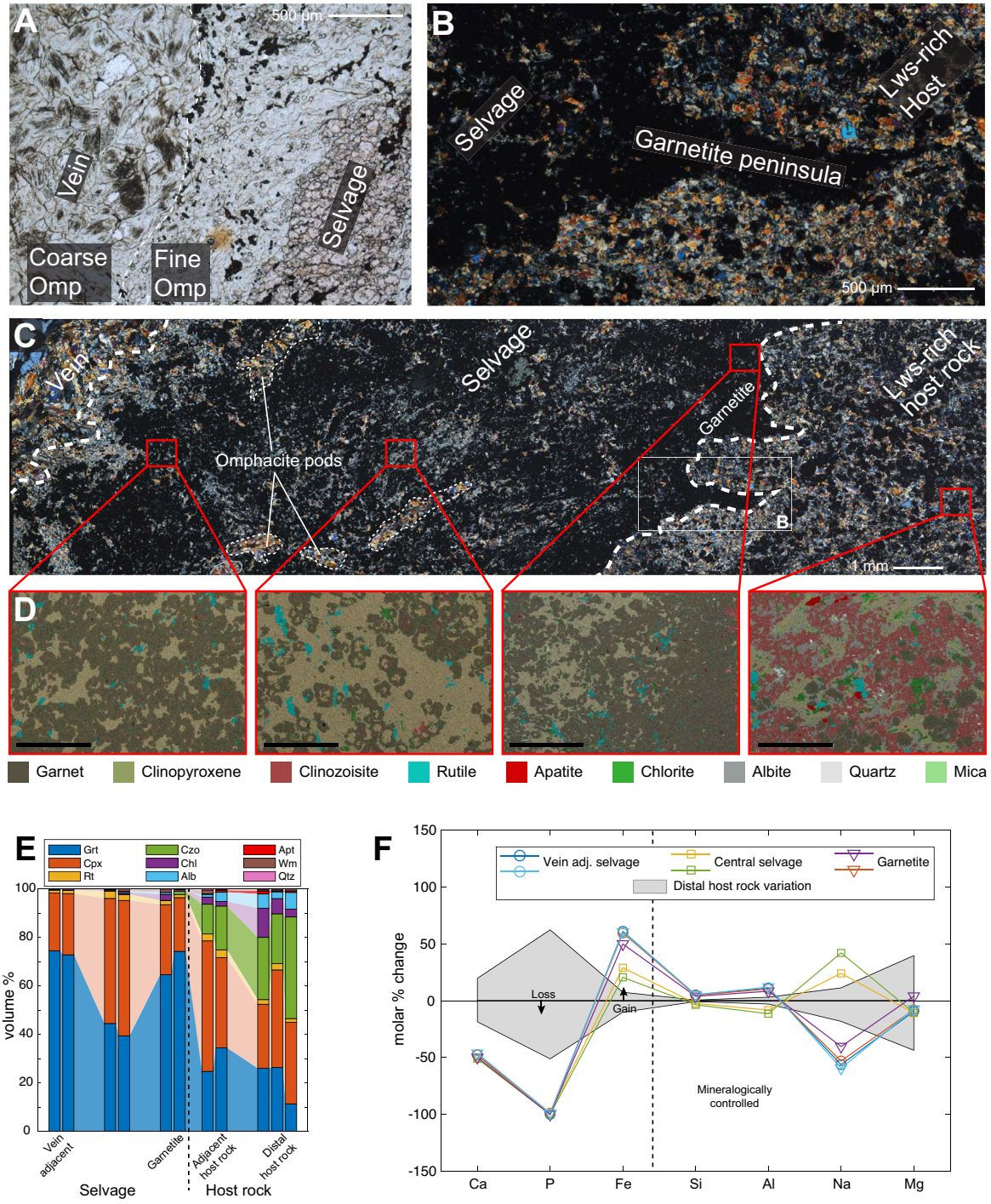

Fig. 6. (A) Plane-polarized light photomicrograph of the vein–selvage transition. The vein–selvage boundary is defined by a change in the texture of omphacite from coarse-to fine-grained. This contact is lined with rutile. The main selvage begins with the appearance of abundant garnet. (B) Cross-polarized light photomicrograph of garnetite at the host rock–selvage boundary showing peninsular structures penetrating into the host rock. (C) Composite cross-polarized light photomicrograph of the entire selvage showing the variation in garnet abundance. The location of (B) is marked by the white box and analogous locations for the phase maps in (D) are marked by red boxes. White lines outline host rock–selvage and vein–selvage boundaries and omphacite pods within the selvage. (D) Phase maps of the selvage and Lws-rich host rock constructed by overlaying multiple elemental maps. The clear distinction in lawsonite (approximated as clinozoisite) and garnet abundance between host rock and selvage is apparent. The variable garnet abundance across the selvage visible in (C) is also visible here. (E) Modal abundance across the selvage and host rock calculated from pixel counting of phase maps. Dashed line marks the selvage–host rock boundary. Paired bars were calculated from different maps at similar positions within the selvage and host rock. The three distal host rock maps were collected on a separate thin section. (F) Mass balance of major elements across the selvage assuming constant volume using bulk compositions calculated from measured mineral compositions and modal abundance. Percent change is calculated on a molar basis relative to the mean of the distal Lws-rich host rock. The gray area encompasses the variability of the distal Lws-rich host rock. Fluid infiltration appears to have driven the loss of Ca and P and gain of Fe and Mn. Variable changes in Na, Al and Si appear to scale with garnet abundance (see E) and likely reflect local mineralogical redistribution.

Table 3: Quantitative modal abundance (volume %) variations across the selvage and in the Lws-rich host rock derived from chemical maps

	Selvage						Lws-rich host rock				
	Vein adjacent		Central selvage		Garnetite		Selvage adjacent		Distal host rock		
Garnet	74	73	44	39	65	74	25	34	26	26	11
Clinopyroxene	24	25	52	56	29	22	54	37	26	40	34
Rutile	1.3	1.4	3.1	2.4	1.8	1.3	2.8	3.2	1.9	2.6	1.5
Clinozoisite	nd	nd	0.1	0.1	tr	1.3	12	18	26	21	42
Chlorite	0.3	0.6	0.5	0.7	2.5	0.8	2.9	1.9	12	6.3	3.2
Albite	nd	nd	0.2	0.5	0.8	tr	1.2	3.8	5.9	2.8	6.9
Apatite	nd	tr	tr	nd	nd	tr	0.2	0.8	1.3	0.4	0.6
White mica	0.2	nd	nd	1.0	1.4	0.2	1.5	0.4	0.5	0.5	0.8
Quartz	nd	nd	0.1	tr	0.1	tr	0.5	0.3	0.4	0.4	tr

nd, not detected; tr, trace (<0.1%)

relative to the vein (Table 2, Fig. 6C). Apatite occurs in the selvage almost exclusively within these pods. Observations in thin section and hand sample suggest that the selvage both truncates, and is traversed by, coarse omphacite pods in the observed 2-D sections suggesting either significant 3-dimensionality to the coarse omphacite pods or complex temporal relationships between these features (Fig. 2). Branches splaying off the main vein are texturally similar to the omphacite pods in the selvage but are not observed in direct continuity (Figs. 5E and 7E).

METHODS

Scanning electron microscopy

Semi-quantitative chemical maps used to create phase maps and calculate modal abundance were collected at the University of Washington using the Thermo-Fisher/FEI Apreo-S with Lovac multi-vacuum field-emission scanning electron microscope (FE–SEM) with an Ultimax 100 large area Analytical Silicon Drift energy dispersive spectroscopy (EDS) detector. All mappings were performed with an accelerating voltage of 20 kV, beam current of 800 pA, dwell time of 50 μs and pixel size of 1.3 μm. Each map was collected as three consecutive frames under these conditions for a total dwell time of 150 μs on each pixel. Phase maps were constructed by stacking EDS maps with each element tied to a different color channel. Modal abundance by area (assumed to be volume) was calculated by pixel counting of these phase maps and converted to modal abundance by mass using the density of each phase. Modal abundance by mass was converted to a molar basis using the molar mass of each phase, calculated either from average mineral compositions for the Lws-rich host and selvage (garnet, clinopyroxene, apatite and clinozoisite), or assuming ideal compositions (rutile, albite, chlorite, muscovite for phengite and quartz). Molar bulk compositions for each mapped region were calculated using the molar abundance from EDS maps and the molar composition of each phase measured by EPMA. For mass balance calculations, the mean composition of the three distal host rock regions was assumed as the initial composition and the variability of the distal host rock bulk compositions was taken as the uncertainty in the mass balance. Calculations were made assuming constant volume given that no trace element measurements were available for use as an immobile reference frame.

Electron probe microanalysis

Major elements were measured in apatite, garnet, clinopyroxene and clinozoisite with the JEOL JXA-8900R Superprobe at the University of Maryland by wavelength-dispersive spectroscopy with a ZAF correction (Armstrong, 1988). All analyses were performed utilizing an accelerating voltage of 15 kV and a cup current of 10 nA. Beam diameter was 1 μm for garnet analyses, 2 μm for clinopyroxene and clinozoisite analyses and 10 μm for apatite. The following crystals were used: LDE1 (F), PET (Cl, S, Ca, P), TAP (Na, Mg, Si, Sr, Al) and LiF (La, Ce, Mn, Fe). K-series x-ray lines (k_α) were utilized for all elements except La, Ce and Sr in apatite where L-series lines were used (L_α). Peak and background were measured for each of the elements. Peak and background count times for the halogens and sulfur were up to 60 s and 10 s, respectively: the majority of the remaining elements were counted for 20 s on peak and 5 s on background. Chemical maps of garnet were collected with a 250-nA cup current, 15 kV accelerating voltage, 1 μm beam diameter, 100 ms dwell time and pixel size of 0.8 μm. Chemical maps of apatite and associated clinopyroxene inclusions were collected with a 113 nA cup current, 15 kV accelerating voltage, 1 to 3 μm beam diameter, 50 ms dwell time and pixel sizes from 1 to 3 μm.

Measurement of halogen contents in apatite by electron probe microanalyzer is challenging because of the mobility of halogens under the electron beam among other complicating factors. To minimize this effect, a large beam diameter of 10 μm was used and F, Cl and Na were analyzed first followed by the remaining elements. Further details on the methodological approach are given by Piccoli & Candela (1994). Standards for apatite analysis were: Durango Apatite-USNM 104021 (Ca, P, F); Scapolite-USNM R6600–1 (Cl, S, Si); Kakanui Hornblende-USNM-143965 (Na, K, Al, Mg, Fe, Al); Strontianite-USNM-R10065 (Sr); Broken Hill Rhodonite-USGS PXBX (Mn), and synthetic LaPO4 (La) and CePO4 (Ce).

Due to the prevalence of inclusions and the fine-grained, intergrown texture of many analyzed phases, a data filtering protocol was used to remove analyses contaminated by inclusions or adjacent phases. Given the absence of unusual end-members in the well-characterized Fe–Ti metagabbros of the Monviso Ophiolite (e.g. Spandler *et al.*, 2011; Locatelli *et al.*, 2018; Locatelli *et al.*, 2019b) and lack of systematic patterns in excluded analyses we feel this is a reasonable approach. For apatite, analyses with totals below 94% or above 100%, or $SiO_2 > 1$ wt.% were discarded. For clinopyroxene, analyses with totals below 96%, $SiO_2 < 50$ wt.% or > 60 wt.%, or $TiO_2 > 1$ wt.% were discarded. Garnet analyses with totals below 98%, $SiO_2 < 36$ wt.%, $Na_2O > 0.3$ wt.%, or $TiO_2 > 1$ wt.% were discarded.

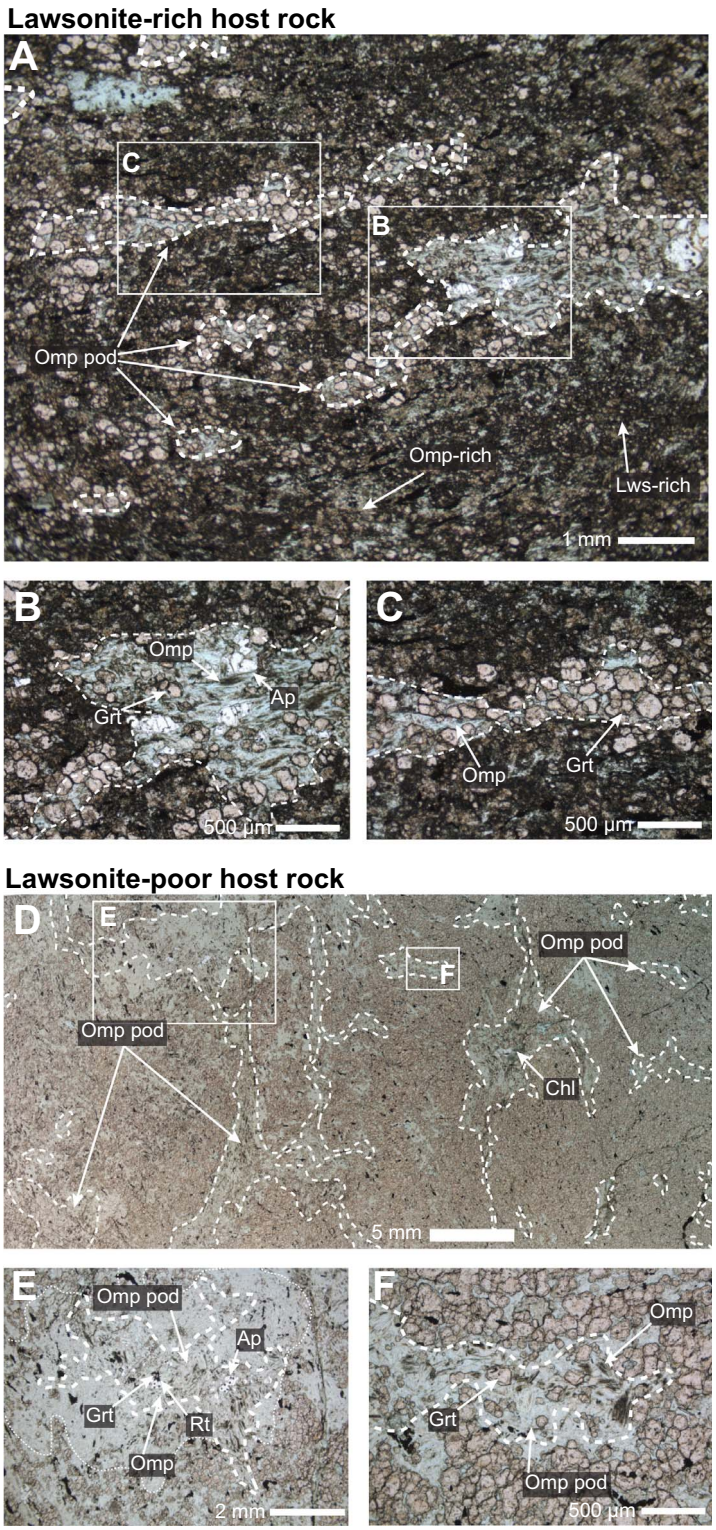

Fig. 7. Plane-polarized light photomicrographs of omphacite pods in both host rock domains. (A) Examples of the morphology of omphacite pods in the Lws-rich host rock. Note their branching and sinuous shape and discontinuity. Omphacite + apatite and garnet + omphacite pod end-members are visible and shown in zoomed-in images in (B) and (C), respectively. Note the subtle heterogeneity in the lawsonite:omphacite ratio in the host rock surrounding the omphacite pods. (B) Example of the omphacite-rich end-member mineralogy of the omphacite pods. Omphacite is coarse and contains clouded cores characteristic of omphacite pods and similar to omphacite in the vein (see Fig. 4C and D). Note the large apatite crystals. (C) Example of garnet-rich end-member mineralogy of the omphacite pods. Note that garnet tends to line the edge of the pod. Abbreviations are Grt, garnet; Omp, omphacite; Ap, apatite; Rt, rutile; Ex-Lws, former lawsonite, from Whitney & Evans (2010). Plane-polarized light photomicrographs of the lawsonite-poor host rock. (D) Distribution of omphacite pods in the Lws-poor host rock showing the characteristic sinuous and branching morphology. (E) Example of a large omphacite pod in the Lws-poor host rock. In contrast to the Lws-rich host rock, a halo of fine-grained omphacite separates the pod (coarse dashes) from the host rock (fine dashes). (F) Small omphacite pod in the Lws-poor host rock with a sharp boundary between host rock and pod. Note the coarse omphacite with cores clouded by dark linear features.

Laser ablation inductively coupled plasma mass spectrometry

Trace element concentrations in apatite, garnet, clinopyroxene and clinozoisite were measured using the Thermo-Fisher Element 2 sector-field inductively coupled plasma mass spectrometer paired with a New Wave Research UP-213-nanometer laser. Spots sizes were 40 to 55 μm for apatite, 30 to 55 μm for garnet and clinopyroxene, and 40 μm for clinozoisite. Repetition rate was 7 Hz for apatite and 10 Hz for other minerals, and fluence was between 2 and 4.5 J/cm^2. The sample surface was cleaned with a few laser shots followed by 30 s of washout, 20 s of on-peak background, 50 s of collection and a 120-s washout. Measurements were made in blocks of up to 18 unknowns bracketed by two standard measurements before and after. The primary standard was NIST610, with Ca (apatite) or Si (silicates) as internal standards, and BHVO-2G as a secondary standard. Data were processed using Iolite 2.5 for apatite and Iolite 4 for silicates (Longerich *et al.*, 1996; Paton *et al.*, 2011; Pettke *et al.*, 2012). Results for secondary standard BHVO-2G reproduced accepted values from the literature (GeoREM database; Jochum *et al.*, 2005) and were within 2SE internal uncertainties. For silicates, contamination from inclusions or adjacent phases was filtered out after data processing based on major (Ca, Al, Na) and trace (P, Ti, Sr, Ce, Lu, Zr) element trends expected for contaminant phases, and concentrations relative to measurements of the same phase and possible contaminants (e.g. garnet: Na for clinopyroxene, Ce, Sr and P for apatite, Ti for rutile, Zr for zircon; clinopyroxene: Ca and Al for clinozoisite, Lu for garnet, Ca, Sr, Ce, P for apatite, Ti for rutile; clinozoisite: Ca and Al for clinopyroxene). Several measurements of clinopyroxene/clinozoisite in the Lws-rich host rock were discarded based on Ca and Al concentrations suggesting mixing between these two phases, consistent with their common intergrowth.

Laser ablation split-stream inductively coupled plasma mass spectrometry

Trace elements and Sr isotope ratios were measured simultaneously in apatite using a laser ablation split-stream system (LASS) at the University of California, Santa Barbara (described in detail in Kylander-Clark *et al.*, 2013). This system pairs a Teledyne CETAC Photon Machines Analyte 193 nm ArF excimer laser and HelEx sample cell with an Agilent 7700X quadrupole inductively coupled plasma mass spectrometer (trace elements) and a Nu Instruments Plasma 3D multi-collector inductively coupled plasma mass spectrometer (Sr isotopes). Ablated material from a single spot was combined in a mixing bulb before being divided and fed into each mass spectrometer for the relevant measurements (split with the majority of ablated volume towards the P3D). Analyses were performed with repetition rate of 10 Hz, a fluence of ~1 J/cm^2, and spot size of 50 μm. An analysis consisted of 2 laser pulses to clean the sample surface, 45 s of washout and on-peak baseline and 30 s of sample analysis. Primary and secondary reference materials (RMs) were measured at the beginning and end of each block of 40 to 80 analyses and alternating after 5 to 10 unknowns throughout the block.

Trace-element measurements were internally standardized using ^{44}Ca and externally standardized with NIST610. All trace-element data were reduced in Iolite 2.5 using the 'internal standard' trace-element data reduction scheme (Paton *et al.*, 2011). Secondary RMs MACS3, BHVO and in-house apatite MAD-UCSB yielded reproducibility within ~10% of expected values. Further information regarding the trace-element method and reproducibility is provided in Edwards *et al.* (2019).

In situ measurement of Sr isotope ratios is complicated by both instrumental mass fractionation and isobaric interferences (Davidson *et al.*, 2007). Measurements by LASS were corrected for mass fractionation to a canonical ^{86}Sr/^{88}Sr ratio of 0.1194 and the isobaric interference on mass 87 by Rb was corrected using the Sr fractionation factor, and ^{87}Rb/^{85}Rb = 0.38571. Masses 84 to 88 (including half-masses to monitor for interferences from doubly charged REE) were collected using 10^{11} Ω amplifiers and a REE correction was applied assuming similar fractionation of doubly charged REE species to that of Sr. Additional details on the multi-collector ICP-MS and LASS method can be found in Edwards *et al.* (2019). The primary RM used for detector bias was MAD-UCSB (^{86}Sr/^{88}Sr = 0.711773) and McClure and Durango apatite were used as secondary RMs (Yang *et al.*, 2014); they yield values within uncertainty of their accepted TIMS values. All ^{87}Sr/^{86}Sr data were reduced using Iolite 2.5 (Paton *et al.*, 2011).

RESULTS

Modal abundance

Six semi-quantitative chemical maps were collected along two transects across the selvage, and five maps were collected within the Lws-rich host rock (Fig. 6D, Data Repository 1). Modal abundances calculated from these maps are consistent with observations of these regions (Tables 2 and 3, Fig. 6C and E). Garnet abundance is higher in the selvage compared with the Lws-rich host rock, and higher at selvage contacts with vein and host rock compared to within the selvage. Apatite and pseudomorphs after lawsonite are nearly absent from the selvage (Fig. 6D and E). Clinopyroxene abundance in the Lws-rich host rock is generally lower than that in the center of the selvage but higher along its contacts where garnet abundance is greater than 80% on a molar basis (Fig. 6E). The Lws-rich host rock also changes adjacent to the selvage contact where garnet and clinopyroxene abundance is higher and clinozoisite (as a proxy for lawsonite) is lower (Fig. 6E).

Major elements

Clinopyroxene in both host rock domains and the vein selvage is omphacite, with 10% to 20% aegirine component (Fig. 8A, Data Repository 2). While omphacite in each of these domains is highly variable ranging from 20% to 50% jadeite component, there are no systematic variations in composition between domains (Fig. 8A). Within each of these domains of the sample, there is also no distinguishable difference between the major element composition of coarse- versus fine-grained omphacite or between core and rim of coarse omphacite. Clinopyroxene in the vein is dominantly omphacite; however, some clinopyroxene inclusions in the apatite seam contain rims of magnesian augite (Fig. 8A).

Garnet is typically anhedral with abundant evidence of resorption-regrowth and healed fractures. Garnet is dominantly almandine with variable proportions of pyrope (5–30%) and grossular end-members (10–30%) and with limited spessartine content (<10%; Fig. 8B, Data Repository 2 and 3). Within grains, spessartine content decreases gradually from core to rim with annular low-magnitude enrichments toward the rim (Data Repository 3). Spessartine contents >4% are found only in the cores of rare large crystals in the host rock (Data Repository 3). The rims of these large host rock garnets overlap in composition with the smaller, more common host rock garnet and the selvage garnetite. These large crystals also tend to have core-to-rim increases in pyrope and high grossular cores increasing toward

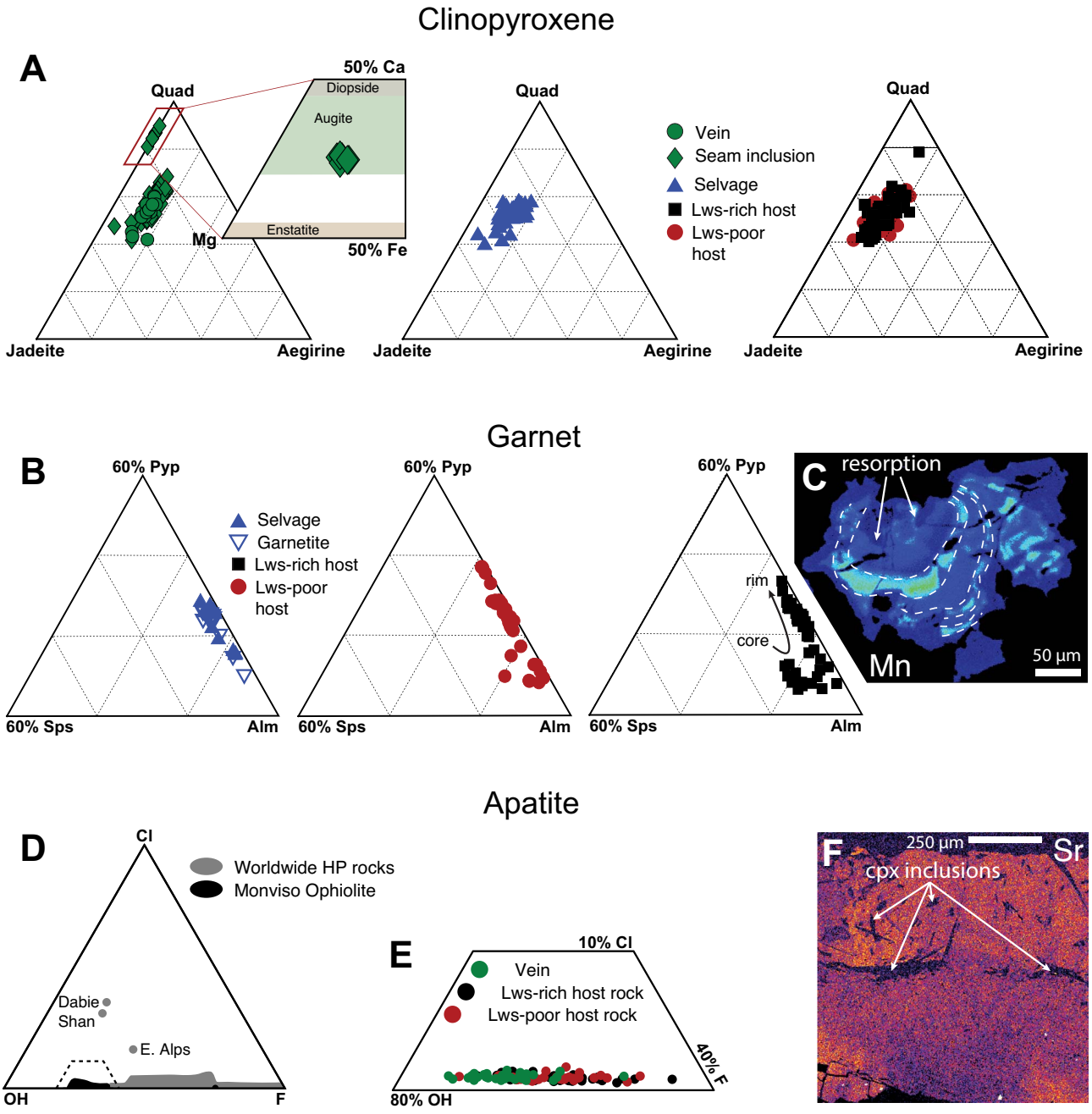

Fig. 8. Major element compositions of clinopyroxene, garnet and apatite. (A) Clinopyroxene ternary diagrams showing the major element compositions of clinopyroxene in different domains of the sample. Clinopyroxene of omphacitic composition overlaps in all domains of the sample. Some vein seam inclusions are magnesian augite. (B) Ternary plots of garnet major element compositions for the selvage and Lws-rich and Lws-poor host rock domains. Host rock garnet overlaps the selvage but extends to higher pyrope and spessartine contents. (C) Manganese map of the lone garnet identified in the vein showing oscillatory zoning suggestive of episodic fluid influx. (D) Ternary plot of halogen content of worldwide high-pressure metamorphic rocks (see text for references) and of Monviso Ophiolite apatite. The Monviso Ophiolite is F-poor relative to all other HP apatite in the literature. (E) In the specific sample studied here, the vein apatite has lower F concentrations relative to the host rock. (F) False-color Sr X-ray chemical map of the apatite seam and associated clinopyroxene inclusions. Strontium-rich zones are patchy with no evidence of concentric zoning. Boundaries between zones are gradual.

a maximum in the mantle then decreasing towards the rim (Data Repository 3). Selvage and small host rock garnets have more complex annular, oscillatory or patchy zonation in both pyrope and grossular potentially related to resorption-regrowth and healed fracturing (Data Repository 3). Garnet in the vein is more extensively resorbed than host rock or selvage garnet and contains oscillatory zonation between ~0.5 and 1.5 wt.% MnO (Fig. 8C; concentration range inferred from measurements on host rock and extrapolated using correlated chemical maps, Data Repository 4).

Apatite in the vein and host rock is 20 to 40% fluorapatite and < 2% chlorapatite with vein apatite having slightly lower fluorapatite contents <30% (calculated as Piccoli & Candela, 2002; Fig. 8D and E, Data Repository 2). Detectable concentrations of Sr, Ce and La were measured in some crystals. Chemical mapping of the vein seam reveals no concentric zoning or zonation

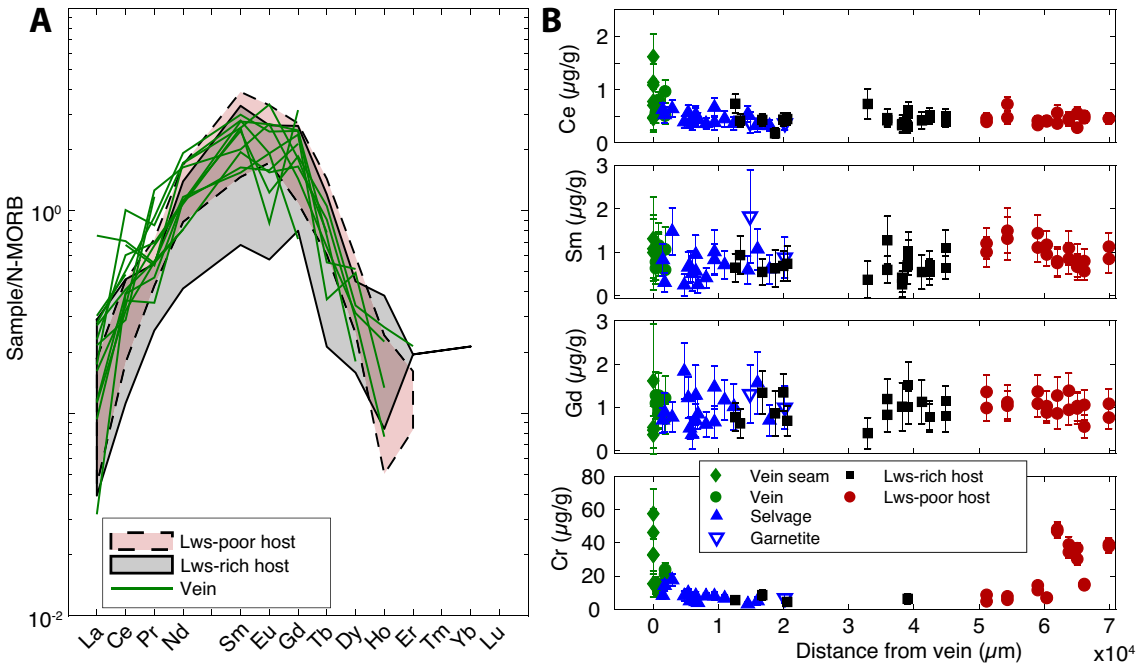

Fig. 9. Trace element compositions of clinopyroxene. (A) N-MORB–normalized REE plot for clinopyroxene in the host rock domains and the vein, showing slight LREE enrichment in the vein relative to the host rock. (B) Traverses across the sample for REE and Cr showing the enrichment in the vein and progressive decrease across the selvage to background concentrations in the host rock. A decrease in REE concentration is unresolvable for the MREE relative to the host rock variability.

relative to the vein wall, but irregular diffuse zoning is present in Sr (Fig. 8F).

Clinozoisite in lawsonite pseudomorphs throughout the sample is >90% to ~45% clinozoisite with Fe content increasing toward the rims (Data Repository 2).

Trace elements

Clinopyroxene

Clinopyroxene in all domains of the sample is enriched in MREE relative to N-MORB with convex-up patterns symmetrical around Sm and Eu (Fig. 9A, Data Repository 4). Vein clinopyroxene REE concentrations, both seam inclusions and in the main portion of the vein, broadly overlaps the host rock but with a slight LREE enrichment in some crystals (Fig. 9A). Concentration of LREE (lighter than Nd) decrease across the selvage with distance from the vein (Fig. 9B). Vein clinopyroxene and Lws-poor host rock omphacite are enriched in Cr relative to all other domains of the sample, and concentrations in selvage omphacite decrease with distance from the vein (Fig. 9B). Few analyses of the Lws-rich host rock returned Cr concentrations above the detection limit (Fig. 9B, Data Repository 4).

Garnet

Garnet in all domains of the sample is enriched in M + HREE heavier than Nd compared with N-MORB (Fig. 10A, Data Repository 4). REE concentrations of all domains in the sample overlap (Fig. 10B). Concentrations of Y, REE and Sc are enriched in rims compared to cores in garnet from the Lws-rich host rock (Fig. 10C). However, a single high-HREE analyses (~18 μg/g Lu, ~80 μg/g Yb) in one Lws-rich host rock garnet core suggests that the thin section plane may miss narrow HREE enrichment in the morphological center of many garnets (Fig. 10C, Data Repository 4; e.g. Skora *et al.*, 2006). In contrast, the Lws-poor host rock shows no systematic core-rim variation (Fig. 10C). Selvage garnet and garnetite peninsulas are comparable in Y + REE and Sc concentration to Lws-rich host rock garnet rims (Fig. 10C). Chromium is rarely present above detection limit in garnet, and only in the Lws-poor host rock (>30 μg/g) and the selvage (<10 μg/g; Data Repository 4).

Apatite

Apatite is enriched in all REE relative to N-MORB and in LREE over HREE with a peak in normalized REE plots at Sm (Fig. 11A, Data Repository 4). The Lws-rich and -poor host domains broadly overlap in REE concentrations but vein apatite, in both the seam and the main portion of the vein, is enriched by up to a factor of two in L + MREE compared to either host rock domain (Fig. 11A and B). Concentrations of L + MREE decrease in the selvage with distance from the vein, but this trend is unresolvable from host rock variability for REE heavier than Gd (Fig. 11B). In other trace elements, vein apatite is generally more variable and enriched relative to both host rock domains (Fig. 11C and D). REE composition in apatite from the selvage overlaps with both the vein and host rock. Multiple distinct apatite compositions in the vein are distinguishable in Sr, REE, Pb and Th based on vein seam traverses and analyses of isolated crystals in the main vein (Fig. 12, Data Repository 5).

Clinozosite/epidote

Clinozoisite REE concentrations are enriched relative to N-MORB with patterns increasing through the MREE and generally flat across the LREE and HREE (Data Repository 4). The magnitude of LREE enrichment is comparable to that of apatite, while HREE concentrations are slightly lower than in garnet. Concentrations of Sr in clinozoisite approach those in apatite (1600 to 3000 μg/g) and Ti occurs in concentrations >1000 μg/g (Data Repository 4).

Sr isotopes of apatite

Apatite in all domains of the sample broadly overlaps in $^{87}Sr/^{86}Sr$ at relatively un-radiogenic values of 0.7048 to 0.7064 (Fig. 13). No

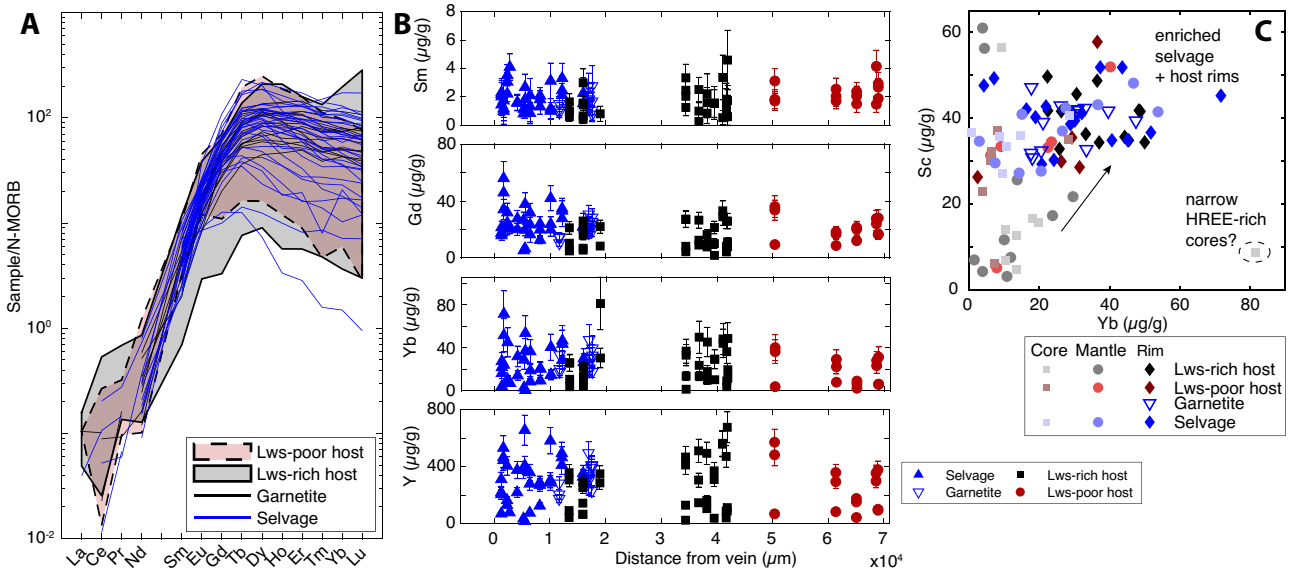

Fig. 10. Trace element compositions of garnet. (A) N-MORB normalized REE plot for garnet showing the relationship between the selvage and two host rock domains. The selvage is generally HREE enriched and shows higher L + MREE compared to the Lws-rich host rock and comparable to the Lws-poor host rock. (B) Traverses for MREE, HREE and Y across the selvage and host rock show no resolvable difference between selvage and host rock. (C) Plot of Sc versus Yb showing core-to-rim variation in these trace elements. Selvage garnet and host rock garnet rims are enriched in these elements relative to the cores and mantles of host rock garnet. In particular, Lws-rich host rock cores and mantles are depleted in all of these trace elements. A single high-Yb analysis in one Lws-rich host rock garnet core suggests this may be in part due to off-center cuts and strong HREE partitioning (e.g. Skora *et al.*, 2006).

variation in $^{87}Sr/^{86}Sr$ with distance across the selvage is resolvable (Fig. 13).

DISCUSSION

Vein-forming fluid source

Geochemical and mineralogical variations in the studied sample are most consistent with vein formation by the infiltration of locally derived fluids transported over a limited, but resolvable distance (>10 cm; Fig. 14). Enrichments in Cr and Ni are a common feature of vein and breccia matrix minerals throughout the Monviso Ophiolite and are interpreted as evidence of serpentinite-derived fluid infiltration (e.g. Spandler *et al.*, 2011; Angiboust *et al.*, 2014; Locatelli *et al.*, 2019b). While vein and selvage clinopyroxene show some modest Cr enrichment in the vein studied here (2–6× host rock; Fig. 9B), these are significantly less than those reported for serpentinite-derived fluids (10–20× mylonitic Fe–Ti metagabbro; Table 1). This suggests vein-forming fluids were not derived from serpentinite in the surrounding LSZ.

The development of a selvage around the studied vein is evidence of incomplete reaction between host rock and a vein-forming fluid that was out of equilibrium with it (Fig. 14). Enrichments of LREE and Cr in vein clinopyroxene and L + MREE and Pb in vein apatite correlate with gradual decreases in these elements in the selvage with distance from the vein (Figs. 9B and 10B). Together with HREE enrichment in selvage garnet relative to host rock garnet cores (Fig. 10C), this suggests that vein fluids added REE, Cr and Pb to the host rock during reaction to form the selvage. Disappearance of lawsonite and apatite from the selvage and increased garnet abundance observed both petrographically and in phase maps suggests selvage formation was also associated with bulk compositional changes (Fig. 6C, D and E). Bulk compositions calculated from phase maps and quantitative mineral compositions suggests reaction between host rock and vein fluids removed Ca and P from the selvage and added Fe (Fig. 6F). Mineralogical changes resulted in the local redistribution of other elements (Na, Al, Si) within the selvage (Fig. 6F). The loss of P and gain of REE observed here is of note as these elements are often observed to show similar patterns of mobilization interpreted as evidence of P complexes mobilizing REE or another agent that complexes both P and REE (e.g. Gieré, 1990; Lee & Byrne, 1992; Ague, 2003; Ague, 2017). Our observation suggests that in this case, the latter is the more likely, and that the complexing agent responsible for transporting REE into the rock may have removed P from the selvage. While the selvage records bulk major and trace element additions and losses associated with fluid–rock reaction, Sr isotopes are homogeneous across the sample suggesting the vein fluid source was local and a similar lithology to the host rock (Fig. 13; e.g. Glodny *et al.*, 2003; Halama *et al.*, 2011; Taetz *et al.*, 2016). This is supported by the lack of resolvable differences in the major element composition of vein, selvage and host rock omphacite (excluding magnesian augite in vein seam inclusions), suggesting limited disequilibrium between host rock and fluid (Fig. 8A; e.g. Angiboust & Raimondo, 2022).

Considering these geochemical patterns, vein-forming fluids were likely derived from metagabbros. Initial stages of eclogite-facies veining and brecciation driven by fluids from adjacent metagabbro involved similar elemental additions (V0 and V1; Table 1) and mineral composition patterns (though without selvage formation around clasts) consistent with our interpreted metagabbro fluid source and suggesting the studied vein formed around peak metamorphism, 2.6 to 2.7 GPa and 550 to 580 °C (Locatelli *et al.*, 2018, 2019b; Angiboust & Raimondo, 2022). However, chemical distinctions between the fluid source rock and vein host rock must have existed to drive selvage formation. Previous studies have reported cm-scale variations in metagabbro mineralogy (both between and within Fe–Ti, Mg–Al and intermediate metagabbro; e.g. Locatelli *et al.*, 2018, 2019b) and oxygen isotopes (Nadeau *et al.*, 1993), and the unaltered portion of the studied sample is particularly lawsonite rich compared to

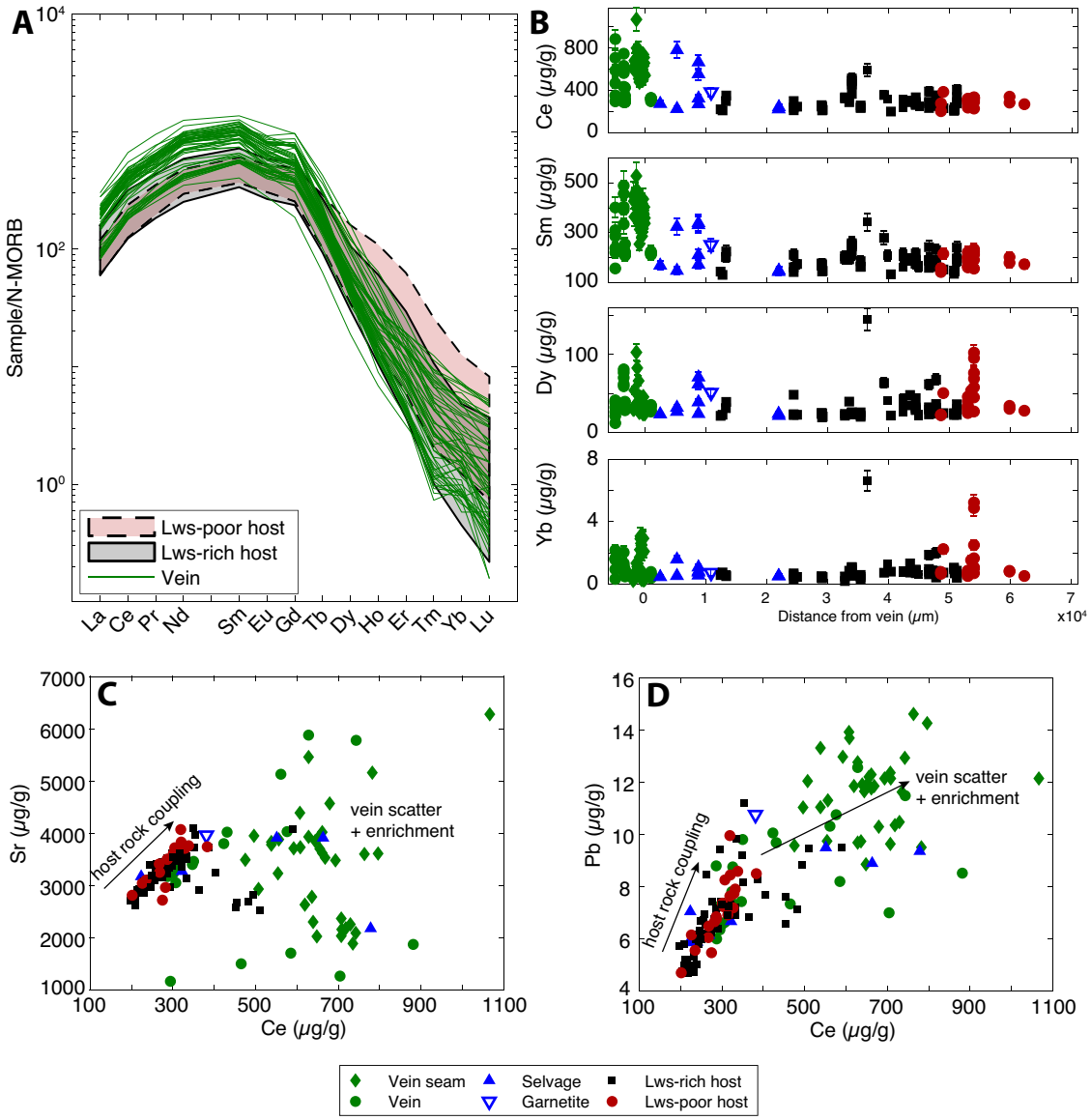

Fig. 11. Trace element compositions of apatite. (A) N-MORB normalized REE plot for apatite in the host rock domains and the vein, showing LREE enrichment in the vein relative to the host rock. (B) Traverses across the sample for REE showing the enrichment in the vein and progressive decrease across the selvage to background concentrations in the host rock (color scheme as in Fig. 2.13). This progressive decrease in concentration is more pronounced for the LREE and the maximum in the vein decreases relative to host rock variability with increasing atomic number. (C and D) Selected plots of apatite trace element compositions showing the general trace element enrichment in the vein seam and single crystals. The vein tends to be more variable and shows marked decoupling of trace elements that are well correlated in the host rock.

typical Monviso Fe–Ti metagabbros (Table 2 and 3; Angiboust *et al.*, 2011, 2012b). These small-scale heterogeneities could have resulted in fluids with higher Fe and lower Ca concentrations relative to that in equilibrium with the host and producing the observed enrichments and depletions in the selvage with no change in mineral major element or Sr isotope composition (Figs. 8 and 13). Given the maximum dimension of Fe–Ti gabbro bodies in this area of the Monviso Ophiolite (Locatelli *et al.*, 2018), fluid transport distances are likely less than a few meters but must be greater than the scale of the hand sample (>10 cm; Fig. 2).

Episodic vein formation

Systematic and resolvable variations in vein mineral chemistry suggest that precipitation resulted from chemically heterogeneous fluids. Episodic fluid transport has been previously inferred for veins, shear zones and breccia networks in the Monviso Ophiolite based on physical evidence (crack seal textures, cross-cutting fractures and breccia generations), oscillatory mineral zoning and oscillatory Li isotope zoning (Philippot, 1987; Spandler *et al.*, 2011; Angiboust *et al.*, 2014; Locatelli *et al.*, 2018, 2019b; Broadwell *et al.*, 2019; Hoover *et al.*, 2022). Likewise, heterogeneity in fluid inclusion daughter mineral assemblages has been interpreted as evidence of variable fluid compositions within single veins (Philippot & Selverstone, 1991). Apatite in the vein seam and isolated vein crystals all contain resolvable variations in Sr, REE and REE ratios that can be correlated between crystals (Fig. 12). Cross-correlated zones in vein apatite can be hundreds of microns wide and separated by millimeters and are best explained by multiple episodes of mineral precipitation in response to different vein fluid compositions. Decoupling of REE,

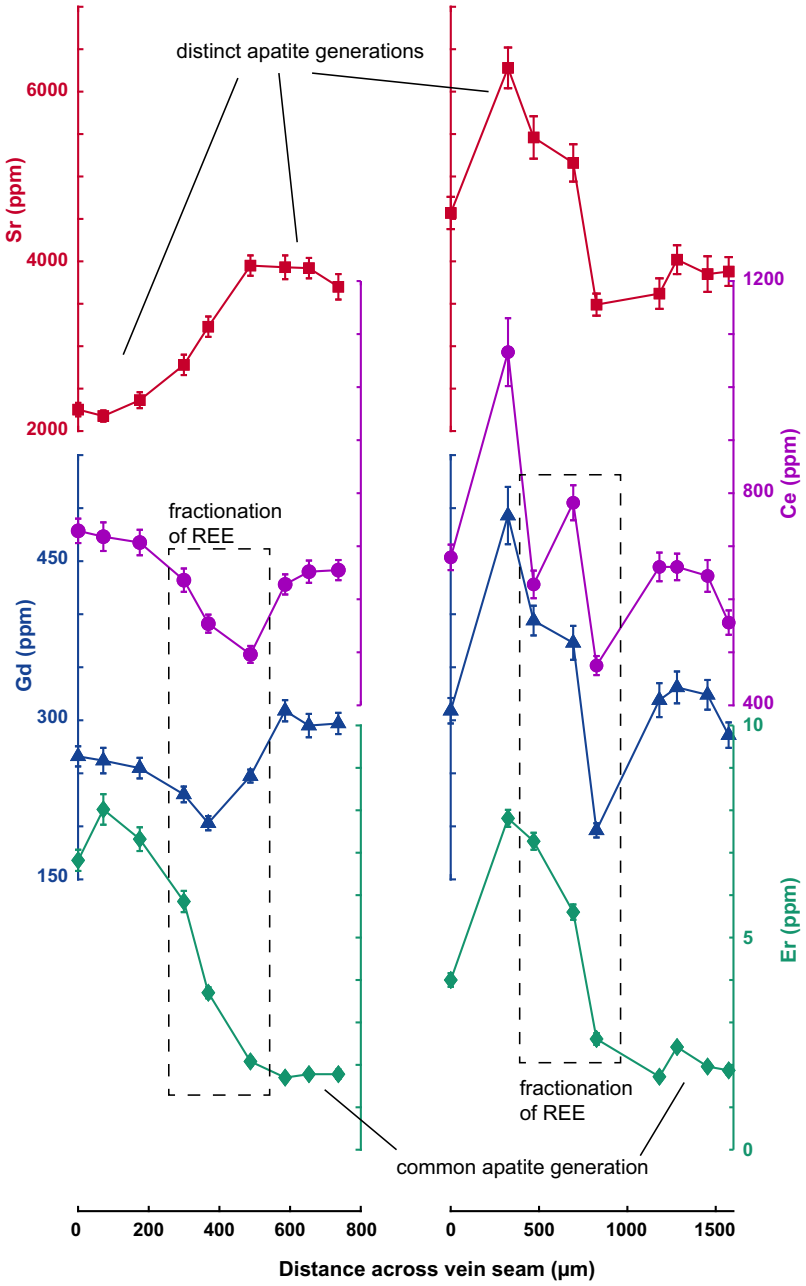

Fig. 12. Apatite trace elements for two traverses measured across the vein seam. Multiple compositional zones are identified based on trace element concentrations. Fractionation of REE may result from diffusion-limited uptake during rapid apatite precipitation.

particularly between cross-correlated regions may reflect a secondary control of growth rate on apatite REE composition (Fig. 12). In garnet REE decoupling has been attributed to crystal growth that outpaces the diffusive supply of REE to the mineral surface resulting in fractionation of LREE and HREE due to their differing diffusivities (Skora *et al.*, 2006). Oscillatory Mn zoning in rare vein garnet (Fig. 8C; Hollister, 1966; Angiboust *et al.*, 2014; Hoover *et al.*, 2022) and linear inclusion arrays in the vein seam (Fig. 5A, B and C) also suggests vein formation was episodic. Based on this textural and chemical evidence in the vein studied here, it appears that even limited local redistribution of fluid among compositionally similar metagabbros occurred in multiples episodes with distinct fluid trace element compositions (Fig. 14).

Fluid–rock disequilibrium as predictor of selvage formation

The alteration selvage developed around the studied vein is the first such feature described in the Monviso Ophiolite and suggests some fundamental difference between the studied sample and previously described clinopyroxene + apatite veins and breccia matrices (Figs. 5 and 6; Philippot, 1987; Spandler *et al.*, 2011; Locatelli *et al.*, 2019b). The reaction selvage around this vein is particularly notable given it involved local transport of fluids sourced from similar lithologies (Figs. 6C and 14), while other features transporting nominally more reactive serpentinite-derived fluids show no evidence of host rock-fluid reaction. The lack of reaction around Cr-rich veins in the ISZ has been attributed to the rapidity of fluid transport, so longer durations of fluid residence

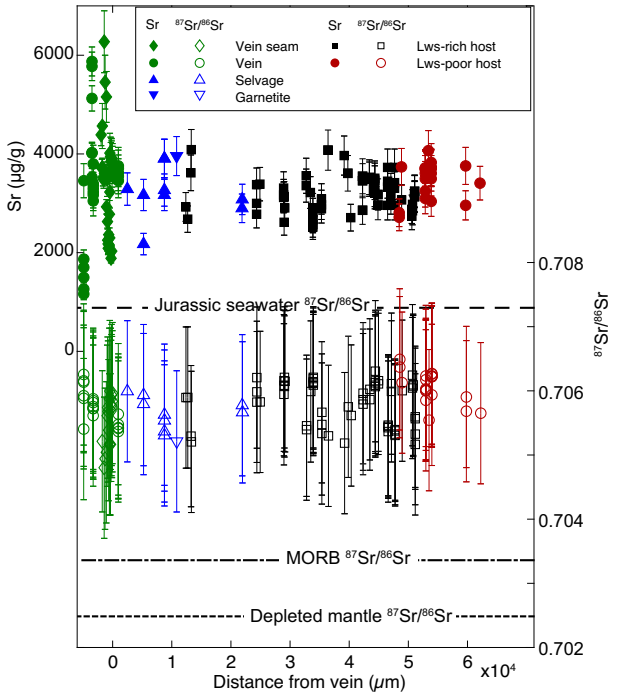

Fig. 13. Apatite Sr concentration and $^{87}Sr/^{86}Sr$ transect across the sample compared to the $^{87}Sr/^{86}Sr$ ratios for Jurassic seawater, MORB and depleted mantle (DM; from Gilio *et al.*, 2020). The vein is highly variable in Sr concentration relative to the host rock but $^{87}Sr/^{86}Sr$ ratios are runiform across the sample suggesting vein fluids were sourced from similar lithologies to the host rock. Plotted uncertainties are 2σ

could explain selvage development in this vein relative to others (Spandler *et al.*, 2011). The studied host rock also contains a higher abundance of lawsonite than typical Fe–Ti metagabbro, and this difference could have also controlled fluid-host rock interaction, either by changing the reactivity or the porosity of the host rock (Figs. 2 and 6D; e.g. Angiboust *et al.*, 2012b). While the relative importance of fluid residence time versus host rock composition cannot be assessed with the data here, the development of vein selvages in the Monviso Ophiolite does not appear to directly depend on the magnitude of fluid–rock disequilibrium but rather suggests a greater importance of other parameters.

Apatite halogen content as a fluid salinity proxy

The halogen composition of apatite from the studied sample overlaps with apatite from other meta-mafic/ultramafic rocks from the Monviso Ophiolite, but all are notably halogen poor relative to apatite from other high-pressure metamorphic rocks (Fig. 8D). Apatite is a common accessory phase in high-pressure metamorphic rocks and metasomatic features (veins and reaction zones); however, it is rarely investigated in detail as a fluid tracer or salinity proxy (e.g. Li & Hermann, 2015). Apatite halogen compositions in HP metamorphic rocks (metasedimentary and metamafic, blueschist to UHP eclogite facies) compiled from the literature are generally Cl poor (<0.4 wt.%) with the exception of a UHP marble from Dabie Shan and an eclogite from the Eastern Alps (Fig. 8D; Svensen *et al.*, 2001; Zack *et al.*, 2002; Marschall, 2005; Gao *et al.*, 2007; John *et al.*, 2008; Beinlich *et al.*, 2010; Guo *et al.*, 2012; Konzett *et al.*, 2012; Li *et al.*, 2013; Guo *et al.*, 2015; Li & Hermann, 2015; Pagé *et al.*, 2016; Liu *et al.*, 2017). Apatite from HP rocks is also characterized by >37% fluorapatite end-member with many localities containing near-end-member fluorapatite (Fig. 8D). Compared to these other localities, apatite from a range of mafic and ultramafic lithologies in the Monviso Ophiolite (Fe–Ti metagabbro block and metasomatic reaction rind, talc- and chlorite-schists, apatite in this clinopyroxene + apatite vein) is uniformly F-poor (Fig. 8D). Fluorapatite content in Monviso apatite ranges from 23% to 37% (with the exception of one metasedimentary sample that is 75% fluorapatite; Li & Hermann, 2015), making it the most F-poor apatite reported to date from HP metamorphic rocks. It is also low in Cl, with a maximum concentration of 0.22 wt.%, and most falling below 0.1 wt.%.

While in some cases, other Cl-bearing phases make the extrapolation from apatite halogen content to fluid salinity complicated (e.g. amphibole in talc- and chlorite-schist), in the studied clinopyroxene + apatite vein, the absence of any other Cl-bearing phases simplifies the relationship between apatite Cl concentration and fluid salinity (Fig. 6D and E). Given the limited fluid transport distances and negligible temperature gradients, the low Cl concentrations in the vein apatite can only be produced by a low-salinity fluid (Brenan, 1993; Urann *et al.*, 2020). While F fluid/apatite partitioning is more complex, the uniformly low F and Cl contents in all analyzed apatite from a range of Monviso lithologies suggests that this locality is halogen-poor, and unusually F-poor, relative to worldwide HP metamorphic rocks. This is in agreement with the lower end of salinities reported in fluid inclusion studies from omphacite veins and breccia matrices in the Monviso Ophiolite (5–29 wt.% NaCleq; Philippot & Selverstone, 1991; Li & Hermann, 2015; Herviou *et al.*, 2021). However, the low apatite halogen concentrations are particularly interesting given the clear evidence in vein minerals and fluid inclusion daughter phases for the mobility of nominally immobile elements, such as REE, Zr, Cr and Ti, including rutile needles in the vein studied here (Fig. 5B; Philippot & Selverstone, 1991; Rubatto & Hermann, 2003; Spandler *et al.*, 2011). Mobility of these elements is often linked to F- and Cl-complexes experimentally shown to increase their solubility; however, in the Monviso Ophiolite, other complexes (e.g. Na-Al-Si, sulfur, phosphorus, yttrium) may have been more important (e.g. Gieré, 1990; Lee & Byrne, 1992; Ayers & Watson, 1993; Ague, 2003; Rapp *et al.*, 2010; Ague, 2017).

Vein precipitation mechanisms

Apatite is a ubiquitous fluid-precipitated phase in the Monviso Ophiolite occurring in veins, breccia matrices and reaction rinds (e.g. Angiboust *et al.*, 2014; Locatelli *et al.*, 2019b; Hoover *et al.*, 2022); however, experimental data suggest that it is relatively insoluble in aqueous fluids (e.g. Ayers & Watson, 1991;Antignano & Manning, 2008a, 2008b ; Mair *et al.*, 2017). Anhydrite, fluorite, calcite, wollastonite and zircon are all more soluble than apatite in aqueous fluids, and precipitation of the observed volume of apatite is difficult to account for with reported metamorphic fluid fluxes (Fig. 5A; Ague, 2014). In addition, experiments indicate that natural apatite will often incongruously dissolve leaving REE sequestered in monazite, inconsistent with the mobility of P and REE associated with vein formation, and the absence of exsolved or residual monazite in the selvage (Figs. 6D and F, 9B, 10B and 11B; e.g. Harlov *et al.*, 2003; Harlov *et al.*, 2005). Given these results on apatite behavior in aqueous fluids, specific conditions can be outlined under which the mobility of large volumes of apatite recorded by the studied vein is possible. Identified mechanisms for dissolution and precipitation of apatite during fluid–rock interaction, based on experiments and natural samples, are as follows:

1) pressure solution,

2) changing pH (e.g.Ayers & Watson, 1991 ; Mair *et al.*, 2017),

3) changing fluid salinity or alkalinity (e.g. Antignano & Manning, 2008a, 2008b; Mair *et al.*, 2017),

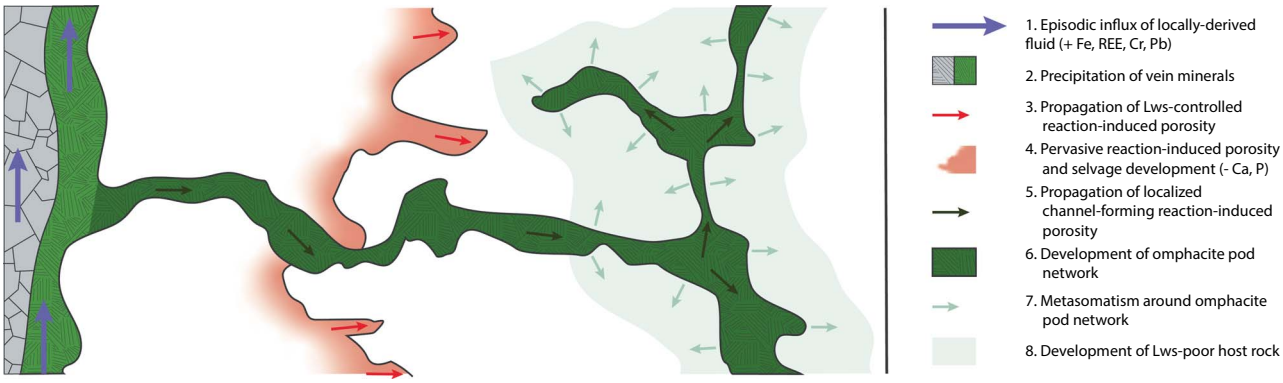

Fig. 14. Conceptual model (not to scale) of the hierarchical metasomatic network formed as the result of reaction-induced porosity development during lawsonite consumption. Fluid infiltration in a fracture in the rock resulted in precipitation of the clinopyroxene + apatite vein. Porosity developed during the consumption of lawsonite accommodated the pervasive metasomatism recorded by the selvage. Local variations in mineral assemblage resulted in the peninsular garnetite structures. Highly localized channel-forming reaction-induced porosity resulted in the formation of the omphacite pod network throughout the host rock and likely represents a more-localized expression of lawsonite-controlled porosity development. Metasomatism immediately adjacent to omphacite pods results in complete alteration of the host rock to form the Lws-poor host rock from the initial Lws-rich host rock.

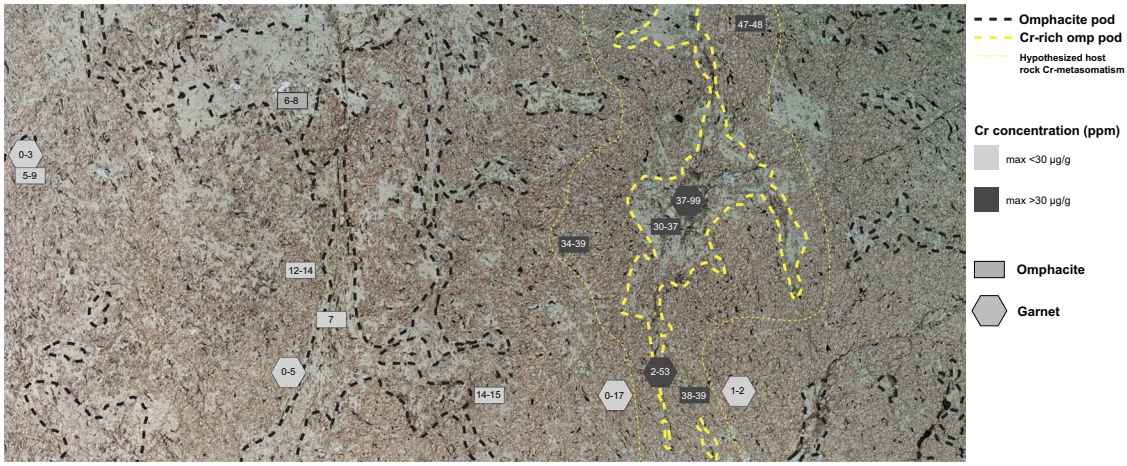

Fig. 15. Thin section map of the Lws-poor host rock showing the distribution of omphacite and garnet Cr concentrations relative to the omphacite pod network. High Cr concentrations are found within or adjacent to a single omphacite pod lineament (outlined in thick yellow line). Enrichment in the host rock surrounding this pod suggests that the pod network facilitated localized but pervasive metasomatism of original Lws-rich host rock to produce the Lws-poor host rock (thick yellow line). The absence of high Cr concentrations in all omphacite pods could reflect multiple fluid infiltration episodes consistent with vein seam apatite trace element variations, oscillatory garnet zoning and vein textures.

4) changing Ca chemical potential (e.g. Ayers & Watson, 1991).

Pressure solution and pH

Pressure solution is unlikely as a driver for apatite mobilization given the lack of ductile deformation in the studied sample (Fig. 2). Apatite solubility has a strong inverse relationship with fluid pH (Ayers & Watson, 1991; Mair *et al.*, 2017). An initially low pH fluid carrying dissolved phosphate could have deposited that phosphate as apatite if the fluid pH was changed by fluid–rock reaction or fluid mixing. However, given the limited disequilibrium between fluid and rock in this system, a large change in pH is unlikely as a driver for apatite dissolution and precipitation.

Fluid salinity

Apatite solubility is dependent on the NaCl and KCl content of the fluid, increasing with KCl, and even more with NaCl concentration (Antignano & Manning, 2008a, 2008b; Mair *et al.*, 2017). Thus, a saline fluid carrying dissolved apatite could precipitate the vein apatite through dilution or loss of dissolved salts. Fluid inclusion studies suggest the upper range of fluid salinities in the Monviso Ophiolite could be consistent with phosphate mobility. In this case, low vein apatite Cl concentrations could be explained by dilution of the vein fluid during fluid–rock interaction (Fig. 8D and E). The dilute fluid salinities inferred from vein apatite would then represent precipitation conditions that differed from initially more saline conditions that mobilized apatite and are represented in fluid inclusion salinities from other Monviso omphacite veins. A role for salinity in apatite mobility is supported by the presence of rutile in the vein, which is typically considered an 'immobile' element in aqueous fluid except in the presence of Cl and F (Fig. 5B; Ayers & Watson, 1993; Rapp *et al.*, 2010).

Calcium chemical potential

Lastly, a change in the chemical potential of Ca (μCa) in the fluid could increase or decrease apatite solubility (Ayers & Watson, 1991). A low-μCa fluid would induce dissolution of apatite, and subsequent increase in μCa could cause its later precipitation. Formation of the vein selvage in this sample involved the loss of Ca into the fluid, as well as the release of H_2O (Fig. 6F). This suggests that the infiltrating fluid was Ca-poor relative to that

in equilibrium with the host rock, and that fluid–rock interaction increased the Ca concentration in fluid, potentially producing the necessary conditions for apatite precipitation. The presence of low-Na magnesian augite inclusions in the vein apatite seam may record μCa increases and offer further evidence of μCa-driven precipitation (Fig. 8A).

Considering the context of this sample, mobilization of apatite (and rutile) into the fluid was likely initially accomplished with relatively saline (up to 28 wt.% NaCleq, mean ~15 wt.% NaCleq; Herviou *et al.*, 2021) and Ca-poor fluids. Reaction of this fluid with the lawsonite-rich host rock drove dissolution of lawsonite that resulted in both dilution of the fluid via released H_2O and an increase in the Ca concentration producing higher Ca chemical potentials and low salinities necessary to precipitate apatite (and rutile; Fig. 6D, E, and F). However, even under conditions in which apatite and rutile can be mobilized in an aqueous fluid, the fluid fluxes necessary to precipitate the large quantities of either mineral (cm-scale rutile needles and large apatite seam; Figs. 2 and 5) seem to be inconsistent with the locally derived fluids and limited vein size. One mechanism that could account for this discrepancy is long-residence fluids, which have been shown to facilitate element mobility in subduction zone and contact metamorphic vein systems by acting as a long-term fast diffusion pathway rather than carrying elements via advection (e.g. Widmer & Thompson, 2001; Bégué *et al.*, 2020).

Reaction-induced porosity

Both the garnetite peninsulas at the selvage–host rock interface and the omphacite pods distributed throughout the selvage and host rock preserve heterogeneities in the spatial distribution of fluid–rock interaction (Fig. 14). The host rock–selvage boundary is a reaction interface where peninsular irregularities reflect mm-scale variations in reaction rate controlled by the physical parameters of fluid–host rock interaction. Similarly, omphacite pods are texturally and chemically distinct from the surrounding host rock and selvage suggesting a fluid-related origin. However, their web-like distribution is inconsistent with formation as veins by fracturing and mineral precipitation, rather they reflect even greater localization and acceleration of reaction rate. This evidence of spatial heterogeneities in reaction are comparable to other metasomatic and metamorphic settings. In contact metamorphism, irregular reaction interfaces have been observed from mm- to m-scale and interpreted as differences in reactivity (e.g. Ferry *et al.*, 2005), reacting rock permeability (e.g. Ferry *et al.*, 2002), or the interaction between the two (reaction-induced porosity; e.g. Yardley & Lloyd, 1995) where mineral reactions result in volume decrease and porosity generation facilitating further fluid infiltration and reaction. In metasomatic features from exhumed paleosubduction terranes, Li isotope profiles measured normal to veins transporting reactive fluids are best reproduced with diffusion models that incorporate reaction-induced porosity generation (John *et al.*, 2012; Taetz *et al.*, 2018). The garnetite peninsulas appear to represent a process of pervasive but heterogeneous metasomatism driven by reaction-induced porosity generation comparable to these examples from contact and high-pressure metamorphic settings (Figs. 6B and 14).

More localized metasomatic features comparable to the omphacite pods have been reported from mineral replacement experiments and natural metamorphic dehydration reactions. In experiments where apatite replaces marble under hydrothermal conditions, porosity produced by the replacement reaction initiated along grain boundaries enables fluid infiltration and localized propagation of the reaction (Jonas *et al.*, 2014). Drainage of dehydrating serpentinites in subduction zones has been suggested to occur via reactive porosity that self-organizes into networks of porous 'veins' (here used to describe the morphology of the features without implying fracturing; Plümper *et al.*, 2017). Original heterogeneity in antigorite Fe content is inferred to localize initial dehydration and solid volume loss producing porous channels in these regions that eventually connect to drain the rock without fracturing or pervasive fluid flow. The omphacite pods are best explained as structures analogous to this localized, channel-forming reactive porosity (Figs. 7D and 14).

The garnetite peninsulas and omphacite pods are interpreted as two expressions of reaction-induced porosity and can both be linked to the reaction of lawsonite (Fig. 14). Lawsonite abundance decreases to near-zero across the selvage–host rock interface, and is rare in omphacite pods compared to the Lws-rich host rock, suggesting that it was consumed during fluid–rock interaction and may have been involved in localizing reaction progress (Fig. 6D and E). While in this case lawsonite reaction appears to be metasomatically driven, lawsonite dehydration due to increasing pressure and temperature is known to produce a negative change in solid volume (Abers *et al.*, 2013) and ~4% porosity was formed as vugs in Monviso Fe–Ti metagabbro during prograde dehydration of lawsonite, glaucophane and chlorite (Angiboust & Raimondo, 2022). Micrometer- to millimeter-scale variations in the abundance of lawsonite versus inherited from the Fe–Ti gabbro protolith could explain the rapid and/or preferential reaction of some regions over others (Figs. 3A and B, 6D, 14). In this model, preferential reaction of regions with higher or favorable lawsonite/omphacite ratio drove increased reaction progress and permeability development, creating a positive feedback loop that localized metasomatism to produce the observed garnetite peninsulas and omphacite pod network (Fig. 14). A similar explanation was invoked for the heterogeneous distribution of fluid-filled vugs formed during prograde dehydration in Monviso Ophiolite Fe–Ti metagabbro (Angiboust & Raimondo, 2022). The limited prominence of garnetite peninsulas outward beyond the selvage front suggests that the contrast in their bulk reaction rates was limited, while the omphacite pods appear to have far outpaced any associated pervasive reaction interface (Fig. 14). The different expressions of reaction-induced porosity preserved in the garnetite peninsulas and the omphacite pod network could be the result of different pulses of fluid with distinct chemistry recorded in variable vein apatite trace element compositions (Fig. 12).

Metasomatic origin of the bimodal host rock

Metasomatism within the omphacite pod network may have also resulted in more pervasive alteration of the host rock itself, resulting in the characteristic bimodal mineralogy of the sample (Figs. 2 and 15, Table 2). Apatite disseminated in the matrix in the Lws-rich host rock is absent in the Lws-poor host rock, only occurring as inclusions in garnet (Fig. 3C and D). This pattern cannot be produced by initial heterogeneity in the protolith. Rather, this suggests that apatite originally present during initial garnet growth was later removed from the matrix during metasomatism, similar to the inferred evolution of the vein selvage. Likewise, the loss of lawsonite in favor of increased garnet abundance in the Lws-poor host rock relative to the Lws-rich host rock is also a shared characteristic with the vein selvage (Fig. 3, Table 2 and 3). Lastly, the vein, selvage, omphacite pods and Lws-poor host rock all contain garnet and clinopyroxene with measurable Cr concentrations that are absent from the Lws-rich host rock (Figs. 9B and 15). In the Lws-poor host rock, elevated Cr concentrations are found only

adjacent to garnet- and chlorite-bearing omphacite pods with similar Cr-enriched signatures suggesting some metasomatism of the Lws-poor host rock beyond the textural limits of this omphacite pod (Fig. 15). Given the abundance of omphacite pods within the Lws-poor host rock domain, this local metasomatism around each omphacite pod could have resulted in large-scale metasomatism of the entire host rock domain. Considering the mineralogical and geochemical similarities between demonstrably metasomatic features (selvage, omphacite pods) and the Lws-poor host rock (Figs. 9B, 15), it is likely that the omphacite pod network resulted in small-scale alteration of the host rock that, in aggregate, resulted in wholesale metasomatism and host rock bimodality (Figs. 3, 7D, E and F, 14, 15). While the bimodal host rock directly results from metasomatism around the omphacite pod network, the density of this network in the Lws-poor host rock relative to the Lws-rich host rock reflects initial compositional or textural heterogeneities inherited from the protolith, illustrating the indirect control of inheritance on later metasomatism.

Hierarchical metasomatic system

Taken together, the vein, selvage and omphacite pods form a hierarchical metasomatic system acting at a variety of scales of localization and distances from the vein (Fig. 14). (1) The clinopyroxene + apatite vein reflects >10 cm transport of fluid between chemically distinct regions of Fe–Ti metagabbro. (2) Immediately adjacent to the vein, pervasive reaction of the host rock with vein-forming fluids produce porosity that propagated into the host rock resulting in selvage development. Minor variations in host rock chemistry inherited from the protolith resulted in an irregular reaction interface preserved in the garnetite peninsulas. (3) Localized increases in reaction rate or porosity form a network of channels that penetrate the host rock beyond the selvage reaction front forming the omphacite pods. (4) Small-scale alteration around these pods metasomatizes the host rock via reactions similar to those in the selvage, and in aggregate, results in total metasomatism of the host rock producing the Lws-poor host rock domain. While lawsonite appears to have been the key phase in producing reaction-induced porosity, the variety of metasomatic textures and evidence for episodic influx of fluids of variable composition suggests that the hierarchical metasomatic system may reflect multiple events (Fig. 12; Philippot & Selverstone, 1991; Spandler *et al.*, 2011; Locatelli *et al.*, 2018; Locatelli *et al.*, 2019b). This is supported by selective Cr enrichment in only some omphacite pods suggesting the entire network did not behave as a single homogeneous system (Fig. 15). This multi-scale metasomatic system evolved through the action of micro-scale reaction-induced porosity but accommodated pervasive macroscopic replacement of the original Lws-rich host rock (Fig. 14). Recent work demonstrated that Fe–Ti metagabbro in Monviso had extremely low permeability capable of retaining ~4% fluid-filled porosity over million-year timescales (Angiboust & Raimondo, 2022). In such a system, even small changes in porosity due to metasomatic reactions could result in significant changes in the permeability of the system and its ability to transport or react with fluids.

CONCLUSION

Results from this work demonstrate the potential of apatite to record fluid histories in high-pressure metamorphic rocks. We show that apatite can be a sensitive recorder of multiple fluid compositions in veins as well as providing constraints on fluid salinity. As a ubiquitous accessory phase, it can also be used to constrain (sometimes cryptic) metasomatism. Both Ca chemical potential and fluid salinity likely played a role in apatite mobilization and deposition, but mechanisms for transport and deposition of large volumes of apatite are still unclear in subduction zone settings. More extensive investigation of apatite trace element and halogen concentrations in subduction zone fluid pathways has the potential to reveal new information about fluid composition and source, and the transport and accumulation of insoluble minerals and elements.

Vein precipitation in the studied sample occurred from locally derived fluids that added limited quantities of Fe, REE, Cr and Pb to the host rock. The alteration selvage around this vein is the first such feature reported in the Monviso Ophiolite despite abundant evidence for transport of nominally more-reactive fluids derived from serpentinite. This suggests that selvage development was controlled by factors, such as fluid residence time rather than simply fluid composition. Variable vein apatite trace elements suggest multiple episodes of vein formation in response to distinct fluid compositions. Structures at the selvage–host rock interface (garnetite peninsulas) and within the host rock (omphacite pod network) reflect the development of reaction-induced porosity during lawsonite consumption. This reaction-induced porosity evolved at a range of scales from pervasive (selvage) to localized (omphacite pods). Metasomatism of the host rock around omphacite pods resulted, in aggregate, in wholesale replacement of the Lws-rich host rock by the Lws-poor host rock. Such reaction-induced porosity could be important in facilitating fluid–rock reaction and fluid transport in subducting slabs where permeability is extremely low.

DATA AVAILABILITY

All in situ major and trace element concentrations and strontium isotope ratios presented here are available in the online Data Repository along with contextual data regarding the location of analyses. The compilation of apatite halogen concentrations in high pressure metamorphic rocks is available upon reasonable request from the authors and all data in that compilation are available in the cited literature.

SUPPLEMENTARY DATA

Supplementary data are available at *Journal of Petrology* online.

ACKNOWLEDGEMENTS

W. Hoover thanks Buchanan Kerswell for assistance with collection of this large sample, Lukas Baumgartner for discussions regarding apatite solubility and Michele Locatelli, Samuel Angiboust and Philippe Agard for an introduction to the field area. W. Hoover thanks Richard Ash for assistance with trace element measurements at the University of Maryland. This work was funded by the U.S. National Science Foundation grants OIA-1545903 to S. Penniston-Dorland and EAR-2053033 to W. Hoover.

References

Abers, G. A., Nakajima, J., van Keken, P. E., Kita, S. & Hacker, B. R. (2013). Thermal-petrological controls on the location of earthquakes within subducting plates. *Earth and Planetary Science Letters* **369-370**, 178–187. https://doi.org/10.1016/j.epsl.2013.03.022.

Agard, P. (2021). Subduction of oceanic lithosphere in the Alps: selective and archetypal from (slow-spreading) oceans. *Earth-Science Reviews* **214**, 103517. https://doi.org/10.1016/j.earscirev.2021.103517.

Ague, J. J. (2003). fluid infiltration and transport of major, minor, and trace elements during regional metamorphism of carbonate rocks, Wepawaug schist, Connecticut, USA. *American Journal of Science* **303**, 753–816. https://doi.org/10.2475/ajs.303.9.753.

Ague, J.J. (2014). Fluid Flow in the Deep Crust. In: Holland, H.D. & Turekian, K.K. (eds) *Treatise on Geochemistry* (2nd ed.). Oxford, UK: Elsevier Ltd, pp. 203–247. https://doi.org/10.1016/B978-0-08-095975-7.00306-5.

Ague, J. J. (2017). Element mobility during regional metamorphism in crustal and subduction zone environments with a focus on the rare earth elements (REE). *American Mineralogist* **102**, 1726–1821. https://doi.org/10.2138/am.2017.6130.

Angiboust, S. & Raimondo, T. (2022). Permeability of subducted oceanic crust revealed by eclogite-facies vugs. *Geology* **50**(8), 964–968. https://doi.org/10.1130/G50066.1.

Angiboust, S., Agard, P., Raimbourg, H., Yamato, P. & Huet, B. (2011). Subduction interface processes recorded by eclogite-facies shear zones (Monviso, W. Alps). *Lithos* **127**, 222–238. https://doi.org/10.1016/j.lithos.2011.09.004.

Angiboust, S., Agard, P., Yamato, P. & Raimbourg, H. (2012a). Eclogite breccias in a subducted ophiolite: a record of intermediate-depth earthquakes? *Geology* **40**, 707–710. https://doi.org/10.1130/G32925.1.

Angiboust, S., Langdon, R., Agard, P., Waters, D. & Chopin, C. (2012b). Eclogitization of the Monviso ophiolite (W. Alps) and implications on subduction dynamics. *Journal of Metamorphic Geology* **30**, 37–61. https://doi.org/10.1111/j.1525-1314.2011.00951.x.

Angiboust, S., Pettke, T. T., De Hoog, J. C. M., Caron, B. & Oncken, O. (2014). Channelized fluid flow and eclogite-facies metasomatism along the subduction shear zone. *Journal of Petrology* **55**, 883–916. https://doi.org/10.1093/petrology/egu010.

Antignano, A. & Manning, C. E. (2008a). Erratum to "Fluorapatite solubility in H2O and H2O-NaCl at 700 to 900 °C and 0.7 to 2.0 GPa" [chemical geology 251/1–4 (2008) 112–119]. *Chemical Geology* **255**, 294. https://doi.org/10.1016/j.chemgeo.2008.06.054.

Antignano, A. & Manning, C. E. (2008b). Fluorapatite solubility in H2O and H2O-NaCl at 700 to 900 °C and 0.7 to 2.0 GPa. *Chemical Geology* **251**, 112–119. https://doi.org/10.1016/j.chemgeo.2008.03.001.

Armstrong, J. T. (1988) Quantitative analysis of silicate and oxide minerals: comparison of Monte Carlo, ZAF and phi-rho-z procedures. In: Newbury D. E. (ed) *Microbeam Analysis*. San Francisco, CA: San Francisco Press, pp. 239–246.

Ayers, J. C. & Watson, E. B. (1991). Solubility of apatite, monazite, zircon, and rutile in supercritical aqueous fluids with implications for subduction zone geochemistry. *Philos Trans Phys Sci Eng* **335**, 365–375. https://doi.org/10.1098/rsta.1991.0052.

Ayers, J. C. & Watson, B. (1993). Rutile solubility and mobility in supercritical aqueous fluids. *Contributions to Mineralogy and Petrology* **114**, 321–330. https://doi.org/10.1007/BF01046535.

Barnes, J. D., Penniston-Dorland, S. C., Bebout, G. E., Hoover, W., Beaudoin, G. M. & Agard, P. (2019). Chlorine and lithium behavior in metasedimentary rocks during prograde metamorphism: a comparative study of exhumed subduction complexes (Catalina schist and Schistes Lustrés). *Lithos* **336-337**, 40–53. https://doi.org/10.1016/j.lithos.2019.03.028.

Bebout, G. E. & Barton, M. D. (2002). Tectonic and metasomatic mixing in a high-T, subduction-zone mélange — insights into the geochemical evolution of the slab – mantle interface. *Chemical Geology* **187**, 79–106. https://doi.org/10.1016/S0009-2541(02)00019-0.

Bebout, G. E. & Penniston-Dorland, S. C. (2016). Fluid and mass transfer at subduction interfaces - the field metamorphic record. *Lithos* **240-243**, 228–258. https://doi.org/10.1016/j.lithos.2015.10.007.

Bégué, F., Baumgartner, L. P., Müller, T., Putlitz, B. & Vennemann, T. W. (2019). Metasomatic vein formation by stationary fluids in carbonate xenoliths at the eastern margin of the Bergell intrusion, val Sissone, Italy. *Journal of Petrology* **60**, 2387–2412. https://doi.org/10.1093/petrology/egaa012.

Beinlich, A., Klemd, R., John, T. & Gao, J. (2010). Trace-element mobilization during Ca-metasomatism along a major fluid conduit: Eclogitization of blueschist as a consequence of fluid–rock interaction. *Geochimica et Cosmochimica Acta* **74**, 1892–1922. https://doi.org/10.1016/j.gca.2009.12.011.

Beltrando, M., Compagnoni, R. & Lombardo, B. (2010). (ultra-) high-pressure metamorphism and orogenesis: an Alpine perspective. *Gondwana Research* **18**, 147–166. https://doi.org/10.1016/j.gr.2010.01.009.

Bovay, T., Rubatto, D. & Lanari, P. (2021). Pervasive fluid-rock interaction in subducted oceanic crust revealed by oxygen isotope zoning in garnet. *Contributions to Mineralogy and Petrology* **176**(7). https://doi.org/10.1007/s00410-021-01806-4.

Breeding, C. M., Ague, J. J. & Bröcker, M. (2004). Fluid-metasedimentary rock interactions in subduction-zone mélange: implications for the chemical composition of arc magmas. *Geology* **32**(12), 1041–1044. https://doi.org/10.1130/G20877.1.

Brenan, J. M. (1993). Partitioning of fluorine and chlorine between apatite and aqueous fluids at high pressure and temperature: implications for the F and cl content of high P-T fluids. *Earth and Planetary Science Letters* **117**, 251–263. https://doi.org/10.1016/0012-821X(93)90131-R.

Broadwell, K. S., Locatelli, M., Verlaguet, A., Agard, P. & Caddick, M. J. (2019). Transient and periodic brittle deformation of eclogites during intermediate-depth subduction. *Earth and Planetary Science Letters* **521**, 91–102. https://doi.org/10.1016/j.epsl.2019.06.008.

Castelli, D., Rostagno, C. & Lombardo, B. (2002). Jd-Qtz-bearing metaplagiogranite from the Monviso meta-ophiolite (Western Alps). *Ofioliti* **27**, 81–90.

Cliff, R. A., Barnicoat, A. C. & Inger, S. (1998). Early tertiary eclogite facies metamorphism in the Monviso Ophiolite. *Journal of Metamorphic Geology* **16**(3), 447–455. https://doi.org/10.1111/j.1525-1314.1998.00147.x.

Cruz-Uribe, A. M., Page, F. Z., Lozier, E., Feineman, M. D., Zack, T., Mertz, R. *et al.* (2021). Trace element and isotopic zoning of garnetite veins in amphibolitized eclogite , Franciscan complex , California, USA. *Contributions to Mineralogy and Petrology* **176**, 1–19. https://doi.org/10.1007/s00410-021-01795-4.

Davidson, J. P., Morgan, D. J., Charlier, B. L. A., Harlou, R. & Hora, J. M. (2007). Microsampling and isotopic analysis of igneous rocks: implications for the study of magmatic systems. *Annual Review of Earth and Planetary Sciences* **35**, 273–311. https://doi.org/10.1146/annurev.earth.35.031306.140211.

Duchêne, S., Blichert-Toft, J., Luais, B., Télouk, P., Lardeaux, J.-M. & Albarède, F. (1997). The Lu – Hf dating of garnets and the ages of the Alpine high-pressure metamorphism. *Nature* **387**(5), 3–6.

Edwards, M. A., Jackson, M. G., Kylander-Clark, A. R. C., Harvey, J., Hagen-Peter, G. A., Seward, G. G. E., Till, C. B., Adams, J. V., Cottle, J. M., Hacker, B. R. & Spera, F. J. (2019). Extreme enriched and heterogeneous 87Sr/86Sr ratios recorded in magmatic plagioclase from the Samoan hotspot. *Earth and Planetary Science Letters* **511**, 190–201. https://doi.org/10.1016/j.epsl.2019.01.040.

Errico, J. C., Barnes, J. D., Strickland, A. & Valley, J. W. (2013). Oxygen isotope zoning in garnets from Franciscan eclogite blocks: evidence for rock–buffered fluid interaction in the mantle wedge. *Contributions to Mineralogy and Petrology* **166**, 1161–1176. https://doi.org/10.1007/s00410-013-0915-0.

Ferry, J. M., Wing, B. A., Penniston-Dorland, S. C. & Rumble, D. (2002). The direction of fluid flow during contact metamorphism of siliceous carbonate rocks: new data for the Monzoni and Predazzo aureoles, northern Italy, and a global review. *Contributions to Mineralogy and Petrology* **142**, 679–699. https://doi.org/10.1007/s00410-001-0316-7.

Ferry, J. M., Rumble, D., Wing, B. A. & Penniston-Dorland, S. C. (2005). A new interpretation of centimetre-scale variations in the progress of infiltration-driven metamorphic reactions: case study of carbonated metaperidotite, val d'Efra, Central Alps, Switzerland. *Journal of Petrology* **46**, 1725–1746. https://doi.org/10.1093/petrology/egi034.

Festa, A., Balestro, G., Dilek, Y. & Tartarotti, P. (2015). A Jurassic oceanic core complex in the high-pressure Monviso ophiolite (western Alps, NW Italy). *Lithosphere* **7**(6), L458.1–L458.652. https://doi.org/10.1130/L458.1.

Gao, J., John, T., Klemd, R. & Xiong, X. (2007). Mobilization of Ti–Nb–ta during subduction: evidence from rutile-bearing dehydration segregations and veins hosted in eclogite, Tianshan, NW China. *Geochimica et Cosmochimica Acta* **71**, 4974–4996. https://doi.org/10.1016/j.gca.2007.07.027.

Gieré, R. (1990). Hydrothermal mobility of Ti, Zr and REE: examples from the Bergell and Adamello contact aureoles (Italy). *Terra Nova* **2**, 60–67. https://doi.org/10.1111/j.1365-3121.1990.tb00037.x.

Gilio, M., Scambelluri, M., Agostini, S., Godard, M., Pettke, T., Agard, P., Locatelli, M. & Angiboust, S. (2020). Fingerprinting and relocating tectonic slices along the plate interface: evidence from the Lago Superiore unit at Monviso (Western Alps). *Lithos* **352-353**, 105308. https://doi.org/10.1016/j.lithos.2019.105308.

Glodny, J., Austrheim, H., Molina, J. F., Rusin, A. I. & Seward, D. (2003). Rb/Sr record of fluid-rock interaction in eclogites: the Marun-Keu complex, polar Urals, Russia. *Geochimica et Cosmochimica Acta* **67**(22),4353–4371.https://doi.org/10.1016/S0016-7037(03)00370-3.

Groppo, C. & Castelli, D. (2010). Prograde P-T evolution of a Lawsonite Eclogite from the Monviso meta-ophiolite (Western Alps): dehydration and redox reactions during Subduction of oceanic FeTi-oxide gabbro. *Journal of Petrology* **51**, 2489–2514. https://doi.org/10.1093/petrology/egq065.

Guo, S., Ye, K., Chen, Y., Liu, J., Mao, Q. & Ma, Y. (2012). Fluid-rock interaction and element mobilization in UHP metabasalt: constraints from an omphacite-epidote vein and host eclogites in the Dabie orogen. *Lithos* **136-139**, 145–167. https://doi.org/10.1016/j.lithos.2011.11.008.

Guo, S., Chen, Y., Ye, K., Su, B., Yang, Y., Zhang, L., Liu, J. & Mao, Q. (2015). Formation ofmultiple high-pressure veins in ultrahigh-pressure eclogite (Hualiangting, Dabie terrane, China): fluid source, element transfer, and closed-system metamorphic veining. *Chemical Geology* **417**, 238–260. https://doi.org/10.1016/j.chemgeo.2015.10.006.

Gyomlai, T., Agard, P., Marschall, H. R., Jolivet, L. & Gerdes, A. (2021). Metasomatism and deformation of block-in-matrix structures in Syros: the role of inheritance and fluid-rock interactions along the subduction interface. *Lithos* **386-387**, 105996. https://doi.org/10.1016/j.lithos.2021.105996.

Halama, R., John, T., Herms, P., Hauff, F. & Schenk, V. (2011). A stable (Li, O) and radiogenic (Sr, Nd) isotope perspective on metasomatic processes in a subducting slab. *Chemical Geology* **281**(3–4), 151–166. https://doi.org/10.1016/j.chemgeo.2010.12.001.

Harlov, D. E., Förster, H. J. & Nijland, T. G. (2002). Fluid-induced nucleation of (Y + REE) -phosphate minerals within apatite: nature and experiment. Part I . Chlorapatite. *American Mineralogist* **87**, 245–261. https://doi.org/10.2138/am-2002-2-306.

Harlov, D. E., Wirth, R. & Förster, H. J. (2005). An experimental study of dissolution-reprecipitation in fluorapatite: fluid infiltration and the formation of monazite. *Contributions to Mineralogy and Petrology* **150**, 268–286. https://doi.org/10.1007/s00410-005-0017-8.

Herviou, C., Verlaguet, A., Agard, P., Raimbourg, H. & Lefeuvre, B. (2021). Along-dip variations of subduction fluids: the 30–80 km depth traverse of the Schistes Lustrés complex (Queyras-Monviso, W. Alps). *Lithos* **394-395**, 106168. https://doi.org/10.1016/j.lithos.2021.106168.

Hollister, L. (1966). Garnet zoning : an interpretation based on the Rayleigh fractionation model. *Science* **154**, 1647–1651. https://doi.org/10.1126/science.154.3757.1647.

Hoover, W. F., Page, F. Z., Schulze, D. J., Kitajima, K. & Valley, J. W. (2021). Massive fluid influx beneath the Colorado plateau (USA) related to slab removal and diatreme emplacement: evidence from oxygen isotope zoning in eclogite xenoliths. *Journal of Petrology* **61**(11-12), 1–18. https://doi.org/10.1093/petrology/egaa102.

Hoover, W. F., Penniston-Dorland, S., Baumgartner, L., Bouvier, A.-S., Dragovic, B., Locatelli, M., Angiboust, S. & Agard, P. (2022). Episodic fluid flow in an eclogite-facies shear zone: insights from Li isotope zoning in garnet. *Geology* **50**(6), 746–750. https://doi.org/10.1130/g49737.1.

Inglis, E., Debret, B., Burton, K., Millet, M. A., Pons, M. L., Dale, C. W. *et al.* (2017). The behavior of iron and zinc stable isotopes accompanying the subduction of mafic oceanic crust: a case study from Western Alpine ophiolites. *Geochemistry Geophysics Geosystems* **2**(1), 476–491. https://doi.org/10.2113/2.4.476.

Jochum, K. P., Nohl, U., Herwig, K., Lammel, E., Stoll, B. & Hofmann, A. W. (2005). GeoReM: a new geochemical database for reference materials and isotopic standards. *Geostandards and Geoanalytical Research* **29**, 333–338. https://doi.org/10.1111/j.1751-908x.2005.tb00904.x.

John, T., Klemd, R., Gao, J. & Garbe-Schönberg, C.-D. (2008). Trace-element mobilization in slabs due to non steady-state fluid–rock interaction: constraints from an eclogite-facies transport vein in blueschist (Tianshan, China). *Lithos* **103**, 1–24. https://doi.org/10.1016/j.lithos.2007.09.005.

John, T., Gussone, N., Podladchikov, Y. Y., Bebout, G. E., Dohmen, R., Halama, R., Klemd, R., Magna, T. & Seitz, H. (2012). Volcanic arcs fed by rapid pulsed fluid flow through subducting slabs. *Nature Geoscience* **5**, 489–492. https://doi.org/10.1038/ngeo1482.

Jonas, L., John, T., King, H. E., Geisler, T. & Putnis, A. (2014). The role of grain boundaries and transient porosity in rocks as fluid pathways for reaction front propagation. *Earth and Planetary Science Letters* **386**, 64–74. https://doi.org/10.1016/j.epsl.2013.10.050.

Konrad-Schmolke, M., Halama, R., Wirth, R., Thomen, A., Klitscher, N., Morales, L., Schreiber, A. & Wilke, F. D. H. (2018). Mineral dissolution and reprecipitation mediated by an amorphous phase. *Nature Communications* **9**, 1637. https://doi.org/10.1038/s41467-018-03944-z.

Konzett, J., Krenn, K., Hauzenberger, C., Whitehouse, M. & Hoinkes, G. (2012). High-pressure tourmaline formation and fluid activity in Fe-Ti-rich eclogites from the Kreuzeck Mountains, eastern Alps, Austria. *Journal of Petrology* **53**, 99–125. https://doi.org/10.1093/petrology/egr057.

Kylander-Clark, A. R. C., Hacker, B. R. & Cottle, J. M. (2013). Laser-ablation split-stream ICP petrochronology. *Chemical Geology* **345**, 99–112. https://doi.org/10.1016/j.chemgeo.2013.02.019.

Lee, J. H. & Byrne, R. H. (1992). examination of comparative rare earth element complexation behavior using linear free-energy relationships. *Geochimica et Cosmochimica Acta* **56**, 1127–1137. https://doi.org/10.1016/0016-7037(92)90050-S.

Li, H. & Hermann, J. (2015). Apatite as an indicator of fluid salinity: an experimental study of chlorine and fluorine partitioning in subducted sediments. *Geochimica et Cosmochimica Acta* **166**, 267–297. https://doi.org/10.1016/j.gca.2015.06.029.

Li, J. L., Gao, J., John, T., Klemd, R. & Su, W. (2013). Fluid-mediated metal transport in subduction zones and its link to arc-related giant ore deposits: constraints from a sulfide-bearing HP vein in lawsonite eclogite (Tianshan, China). *Geochimica et Cosmochimica Acta* **120**, 326–362. https://doi.org/10.1016/j.gca.2013.06.023.

Li, W. Y., Teng, F.-Z. & Xiao, Y. (2018). Magnesium isotope record of fluid metasomatism along the slab-mantle interface in subduction zones. *Geochimica et Cosmochimica Acta* **237**, 312–319. https://doi.org/10.1016/j.gca.2018.06.034.

Liu, P., Massonne, H. J., Jin, Z., Wu, Y. & Zhang, J. (2017). Diopside, apatite, and rutile in an ultrahigh pressure impure marble from the Dabie Shan, eastern China: a record of eclogite-facies metasomatism during exhumation. *Chemical Geology* **466**, 123–139. https://doi.org/10.1016/j.chemgeo.2017.06.001.

Locatelli, M. (2017) *Eclogite breccias from Monviso (W. Alps): structural, petrographic and geochemical evidence for multiple rupture stages at intermediate depths in subduction zones*PhD dissertation,. Paris, France: Sorbonne Université.

Locatelli, M., Verlaguet, A., Agard, P., Federico, L. & Angiboust, S. (2018). Intermediate-depth brecciation along the subduction plate interface (Monviso eclogite, W. Alps). *Lithos* **320-321**, 378–402. https://doi.org/10.1016/j.lithos.2018.09.028.

Locatelli, M., Federico, L., Agard, P. & Verlaguet, A. (2019a). Geology of the southern Monviso metaophiolite complex (W-Alps, Italy). *Journal of Maps* **15**, 283–297. https://doi.org/10.1080/17445647.2019.1592030.

Locatelli, M., Verlaguet, A., Agard, P., Pettke, T. & Federico, L. (2019b). Fluid pulses during stepwise brecciation at intermediate subduction depths (Monviso eclogites, W. Alps): first internally then externally sourced. *Geochemistry, Geophysics, Geosystems* **20**, 5285–5318. https://doi.org/10.1029/2019GC008549.

Lombardo, B., Nervo, R., Compagnoni, R., Messiga, B., Kienast, J.-R., Mevel, C., Fiora, L., Piccardo, G. B. & Lanza, R. (1978). Osservazioni preliminari sulle ofioliti metamorfiche del Monviso (Alpi Occidentali). *Rendicontin Societa Italiana di Mineralogia e Petrologia* **34**, 253–305.

Longerich, H. P., Jackson, S. E. & Günther, D. (1996). Laser ablation inductively coupled plasma mass spectrometric transient signal data acquisition and analyte concentration calculation. *Journal of Analytical Atomic Spectrometry* **11**, 899–904. https://doi.org/10.1039/JA9961100899.

Mair, P., Tropper, P., Harlov, D. E. & Manning, C. E. (2017). The solubility of apatite in H2O, KCl-H2O, NaCl-H2O at 800°C and 1.0 GPa: implications for REE mobility in high-grade saline brines. *Chemical Geology* **470**, 180–192. https://doi.org/10.1016/j.chemgeo.2017.09.015.

Marschall, H. R. (2005) *Lithium, Beryllium and Boron in High-Pressure Metamorphisc Rocks from Syros (Greece)*PhD dissertation,. Germany: University of Heidelburg, Heidelburg.

Messiga, B., Kienast, J.-R., Rebay, G., Riccardi, M. P. & Tribuzio, R. (1999). Cr-rich magnesiochloritoid eclogites from the Monviso ophiolites (Western Alps, Italy). *Journal of Metamorphic Geology* **17**, 287–299. https://doi.org/10.1046/j.1525-1314.1999.00198.x.

Miller, D. P., Marschall, H. R. & Schumacher, J. C. (2009). Metasomatic formation and petrology of blueschist-facies hybrid rocks from Syros (Greece): implications for reactions at the slab – mantle interface. *Lithos* **107**(1–2), 53–67. https://doi.org/10.1016/j.lithos.2008.07.015.

Nadeau, S., Philippot, P. & Pineau, F. (1993). Fluid inclusion and mineral isotopic compositions (HCO) in eclogitic rocks as tracers of local fluid migration during high-pressure metamorphism. *Earth and Planetary Science Letters* **114**, 431–448. https://doi.org/10.1016/0012-821X(93)90074-J.

Page, F. Z., Essene, E. J., Mukasa, S. B. & Valley, J. W. (2014). A garnet-zircon oxygen isotope record of subduction and exhumation fluids from the Franciscan complex, California. *Journal of Petrology* **55**, 103–131. https://doi.org/10.1093/petrology/egt062.

Pagé, L., Hattori, K., de Hoog, J. C. M. & Okay, A. I. (2016). Halogen (F, cl, Br, I) behaviour in subducting slabs: a study of lawsonite blueschists in western Turkey. *Earth and Planetary Science Letters* **442**, 133–142. https://doi.org/10.1016/j.epsl.2016.02.054.

Paton, C., Hellstrom, J., Paul, B., Woodhead, J. & Hergt, J. (2011). Iolite: freeware for the visualisation and processing of mass spectrometric data. *Journal of Analytical Atomic Spectrometry* **26**, 2508–2518. https://doi.org/10.1039/c1ja10172b.

Penniston-Dorland, S. C., Sorensen, S. S., Ash, R. D. & Khadke, S. V. (2010). Lithium isotopes as a tracer of fluids in a subduction zone mélange: Franciscan complex, CA. *Earth and Planetary Science Letters* **292**, 181–190. https://doi.org/10.1016/j.epsl.2010.01.034.

Penniston-Dorland, S. C., Bebout, G. E., Pogge von Strandmann, P. A. E., Elliott, T. & Sorensen, S. S. (2012). Lithium and its isotopes as tracers of subduction zone fluids and metasomatic processes: evidence from the Catalina schist, California, USA. *Geochimica et Cosmochimica Acta* **77**, 530–545. https://doi.org/10.1016/j.gca.2011.10.038.

Pettke, T., Oberli, F., Audétat, A., Guillong, M., Simon, A. C., Hanley, J. J. & Klemm, L. M. (2012). Recent developments in element concentration and isotope ratio analysis of individual fluid inclusions by laser ablation single and multiple collector ICP-MS. *Ore Geology Reviews* **44**, 10–38. https://doi.org/10.1016/j.oregeorev.2011.11.001.

Philippot, P. (1987). "Crack seal" vein geometry in eclogitic rocks. *Geodinamica Acta* **1**, 171–181. https://doi.org/10.1080/09853111.1987.11105136.

Philippot, P. & Selverstone, J. (1991). Trace-element-rich brines in eclogitic veins: implications for fluid composition and transport during subduction. *Contributions to Mineralogy and Petrology* **106**, 417–430. https://doi.org/10.1007/BF00321985.

Piccoli, P. & Candela, P. (1994). Apatite in felsic rocks: a model for the estimation of initial halogen concentrations in the bishop tuff (Long Valley) and Tuolumne intrusive suite (Sierra Nevada batholith) magmas. *American Journal of Science* **294**, 92–135. https://doi.org/10.2475/ajs.294.1.92.

Piccoli, P. M. & Candela, P. A. (2002). Apatite in igneous systems. *Reviews in Mineralogy and Geochemistry* **48**, 255–292. https://doi.org/10.2138/rmg.2002.48.6.

Piccoli, F., Vitale Brovarone, A., Beyssac, O., Martinez, I., Ague, J. J. & Chaduteau, C. (2016). Carbonation by fluid – rock interactions at high-pressure conditions : implications for carbon cycling in subduction zones. *Earth and Planetary Science Letters* **445**, 146–159. https://doi.org/10.1016/j.epsl.2016.03.045.

Plümper, O., John, T., Podladchikov, Y. Y., Vrijmoed, J. C. & Scambelluri, M. (2017). Fluid escape from subduction zones controlled by channel-forming reactive porosity. *Nature Geoscience* **10**, 150–156. https://doi.org/10.1038/ngeo2865.

Putnis, A. & Austrheim, H. O. (2011). Fluid-induced processes: Metasomatism and metamorphism. *Geofluids* **10**, 254–269. https://doi.org/10.1002/9781444394900.ch18.

Rapp, J. F., Klemme, S., Butler, I. B. & Harley, S. L. (2010). Extremely high solubility of rutile in chloride and fluoride-bearing metamorphic fluids: an experimental investigation. *Geology* **38**, 323–326. https://doi.org/10.1130/G30753.1.

Rubatto, D. & Angiboust, S. (2015). Oxygen isotope record of oceanic and high-pressure metasomatism: a P-T-time-fluid path for the Monviso eclogites (Italy). *Contributions to Mineralogy and Petrology* **170**, 1–16. https://doi.org/10.1007/s00410-015-1198-4.

Rubatto, D. & Hermann, J. (2003). Zircon formation during fluid circulation in eclogites (Monviso, Western Alps): implications for Zr and Hf budget in subduction zones. *Geochimica et Cosmochimica Acta* **67**, 2173–2187. https://doi.org/10.1016/S0016-7037(02)01321-2.

van Schrojenstein Lantman, H. W., Scambelluri, M., Gilio, M., Wallis, D. & Alvaro, M. (2021). Extensive fluid–rock interaction and pressure solution in a UHP fluid pathway recorded by garnetite, Lago di Cignana, Western Alps. *Journal of Metamorphic Geology* **39**(4), 501–518. https://doi.org/10.1111/jmg.12585.

Schwartz, S., Lardeaux, J.-M., Guillot, S. & Tricart, P. (2000). Diversité du métamorphisme éclogitique dans le massif ophiolitique du Monviso (Alpes occidentales, Italie) the diversity of eclogitic metamorphism in the Monviso ophiolitic complex, western Alps, Italy. *Geodinamica Acta* **13**, 169–188. https://doi.org/10.1016/S0985-3111(00)00112-1.

Skora, S., Baumgartner, L. P., Mahlen, N. J., Johnson, C. M., Pilet, S. & Hellebrand, E. (2006). Diffusion-limited REE uptake by eclogite garnets and its consequences for Lu-Hf and Sm-Nd geochronology. *Contributions to Mineralogy and Petrology* **152**, 703–720. https://doi.org/10.1007/s00410-006-0128-x.

Sorensen, S. S. & Barton, M. D. (1987). Metasomatism and partial melting in a subduction complex: Catalina schist, southern California. *Geology* **15**, 115–118. https://doi.org/10.1130/0091-7613(1987)15<115:MAPMIA>2.0.CO;2.

Sorensen, S. S., Grossman, J. N. & Perfit, M. R. (1997). Phengite-hosted LILE enrichment in Eclogite and related rocks: implications for fluid-mediated mass transfer in Subduction zones and arc magma genesis. *Journal of Petrology* **38**, 3–34. https://doi.org/10.1093/petroj/38.1.3.

Spandler, C., Hermann, J., Faure, K., Mavrogenes, J. A. & Arculus, R. J. (2008). The importance of talc and chlorite "hybrid" rocks for volatile recycling through subduction zones; evidence from the high-pressure subduction mélange of New Caledonia. *Contributions to Mineralogy and Petrology* **155**(2), 181–198. https://doi.org/10.1007/s00410-007-0236-2.

Spandler, C., Pettke, T. & Rubatto, D. (2011). Internal and external fluid sources for Eclogite-facies veins in the Monviso meta-ophiolite, Western Alps: implications for fluid flow in Subduction zones. *Journal of Petrology* **52**, 1207–1236. https://doi.org/10.1093/petrology/egr025.

van der Straaten, F., Schenk, V., John, T. & Gao, J. (2008). Blueschist-facies rehydration of eclogites (Tian Shan, NW-China): implications for fluid–rock interaction in the subduction channel. *Chemical Geology* **255**, 195–219. https://doi.org/10.1016/j.chemgeo.2008.06.037.

Svensen, H., Jamtveit, B., Banks, D. A. & Austrheim, H. O. (2001). Halogen contents of eclogite facies fluid inclusions and minerals: Caledonides, western Norway. *Journal of Metamorphic Geology* **19**, 165–178. https://doi.org/10.1046/j.0263-4929.2000.00301.x.

Taetz, S., John, T., Bröcker, M. & Spandler, C. (2016). Fluid–rock interaction and evolution of a high-pressure/low-temperature vein system in eclogite from New Caledonia: insights into intraslab fluid flow processes. *Contributions to Mineralogy and Petrology* **171**, 90. https://doi.org/10.1007/s00410-016-1295-z.

Taetz, S., John, T., Bröcker, M., Spandler, C. & Stracke, A. (2018). Fast intraslab fluid-flow events linked to pulses of high pore fluid pressure at the subducted plate interface. *Earth and Planetary Science Letters* **482**, 33–43. https://doi.org/10.1016/j.epsl.2017.10.044.

Urann, B. M., Le Roux, V., John, T., Beaudoin, G. M. & Barnes, J. D. (2020). The distribution and abundance of halogens in eclogites: an in situ SIMS perspective of the Raspas complex (Ecuador). *American Mineralogist* **105**, 307–318. https://doi.org/10.2138/am-2020-6994.

Wang, Z., Teng, F., Busigny, V. & Liu, S. (2022). Evidence from HP/UHP metasediments for recycling of isotopically heterogeneous potassium into the mantle. *American Mineralogist* **107**, 350–356. https://doi.org/10.2138/am-2021-7923.

Whitney, D. L. & Evans, B. W. (2010). Abbreviations for names of rock-forming minerals. *American Mineralogist* **95**, 185–187. https://doi.org/10.2138/am.2010.3371.

Widmer, T. & Thompson, A. B. (2001). Local origin of high pressure vein material in eclogite facies rocks of the Zermatt-Saas zone, Switzerland. *American Journal of Science* **301**, 627–656. https://doi.org/10.2475/ajs.301.7.627.

Yang, Y. H., Wu, F. Y., Yang, J. H., Chew, D. M., Xie, L. W., Chu, Z. Y., Zhang, Y. B. & Huang, C. (2014). Sr and Nd isotopic compositions of apatite reference materials used in U-Th-Pb geochronology. *Chemical Geology* **385**, 35–55. https://doi.org/10.1016/j.chemgeo.2014.07.012.

Yardley, B. W. D. & Lloyd, G. E. (1995). Why metasomatic fronts are really metasomatic sides. *Geology* **23**, 53–56. https://doi.org/10.1130/0091-7613(1995)023<0053:WMFARM>2.3.CO;2.

Zack, T. & John, T. (2007). An evaluation of reactive fluid flow and trace element mobility in subducting slabs. *Chemical Geology* **239**, 199–216. https://doi.org/10.1016/j.chemgeo.2006.10.020.

Zack, T., Foley, S. F. & Rivers, T. (2002). Equilibrium and disequilibrium trace element partitioning in hydrous Eclogites (Trescolmen, Central Alps). *Journal of Petrology* **43**, 1947–1974. https://doi.org/10.1093/petrology/43.10.1947.